Article

Molecular sensing of mechano- and ligand-dependent adhesion GPCR dissociation

https://doi.org/10.1038/s41586-023-05802-5

Received: 12 May 2022

Accepted: 6 February 2023

Published online: 08 March 2023

Check for updates

Nicole Scholz[1,3]✉, Anne-Kristin Dahse[1,3], Marguerite Kemkemer[1], Anne Bormann[1], Genevieve M. Auger[1], Fernando Vieira Contreras[1], Lucia F. Ernst[1], Hauke Staake[1], Marek B. Körner[1], Max Buhlan[1], Amelie Meyer-Mölck[1], Yin Kwan Chung[1], Beatriz Blanco-Redondo[1], Franziska Klose[2], Mohamed Ali Jarboui[2], Dmitrij Ljaschenko[1], Marina Bigl[1] & Tobias Langenhan[1]✉

Adhesion G-protein-coupled receptors (aGPCRs) bear notable similarity to Notch proteins[1], a class of surface receptors poised for mechano-proteolytic activation[2–4], including an evolutionarily conserved mechanism of cleavage[5–8]. However, so far there is no unifying explanation for why aGPCRs are autoproteolytically processed. Here we introduce a genetically encoded sensor system to detect the dissociation events of aGPCR heterodimers into their constituent N-terminal and C-terminal fragments (NTFs and CTFs, respectively). An NTF release sensor (NRS) of the neural latrophilin-type aGPCR Cirl (ADGRL)[9–11], from *Drosophila melanogaster*, is stimulated by mechanical force. Cirl-NRS activation indicates that receptor dissociation occurs in neurons and cortex glial cells. The release of NTFs from cortex glial cells requires *trans*-interaction between Cirl and its ligand, the Toll-like receptor Tollo (Toll-8)[12], on neural progenitor cells, whereas expressing Cirl and Tollo in *cis* suppresses dissociation of the aGPCR. This interaction is necessary to control the size of the neuroblast pool in the central nervous system. We conclude that receptor autoproteolysis enables non-cell-autonomous activities of aGPCRs, and that the dissociation of aGPCRs is controlled by their ligand expression profile and by mechanical force. The NRS system will be helpful in elucidating the physiological roles and signal modulators of aGPCRs, which constitute a large untapped reservoir of drug targets for cardiovascular, immune, neuropsychiatric and neoplastic diseases[13].

aGPCRs exhibit elaborate extracellular regions (ECRs) joined to the heptahelical transmembrane (7TM) signalling domain of GPCRs[14] (Extended Data Fig. 1a). aGPCRs engage with ligands that are either fixed within the extracellular matrix or are membrane molecules themselves[14]. Taken together with physiological[9,15–17] and pharmacological observations[18], this has led to the concept that aGPCRs are activated by mechanical force[19,20]. The structural attributes of aGPCRs support this hypothesis. An extracellular aGPCR-specific GPCR autoproteolysis-inducing (GAIN) domain, which is present in all aGPCRs, cleaves a receptor into a heterodimer composed of an NTF and a CTF, which remain non-covalently connected after self-cleavage[5–8,21] (Extended Data Fig. 1a). aGPCRs contain a tethered agonist element (TA, Stachel) as part of the GAIN fold, which is necessary and sufficient for receptor activation[22,23] (Extended Data Fig. 1a). As the TA is concealed within the intact GAIN domain[6], its exposure may be procured through the conformational flexibility of the GAIN domain that allows for TA–7TM domain interactions in receptor heterodimers[9,10,21,23–25] (non-dissociation model; Extended Data Fig. 1b). Alternatively, physical disruption of the heterodimer decrypts the TA and triggers aGPCR activation[22,26] (dissociation model; Extended Data Fig. 1b). Recent structural evidence shows that TA–7TM engagement may occur in autoproteolytically inactive full-length receptors[27] and isolated aGPCR CTFs[28–30]. Hence, receptor self-cleavage and heterodimer dissociation are important for aGPCR signalling (Extended Data Fig. 1b). However, methods for the detection of aGPCR dissociation at cellular and temporal resolution that can be combined with pharmacological and physiological investigations are lacking. Here we introduce a transgenic, bioorthogonal NTF release sensor (NRS) system that reports the separation of aGPCR heterodimers in vitro and in vivo.

Sensor design for aGPCR NTF release

The NRS working principle is based on the molecular events that trigger Notch receptor signalling, which regulates a multitude of developmental processes[31]. In brief, Notch is activated through its adhesive ligands

[1]Rudolf Schönheimer Institute of Biochemistry, Division of General Biochemistry, Medical Faculty, Leipzig University, Leipzig, Germany. [2]Core Facility for Medical Bioanalytics, Institute for Ophthalmic Research, Eberhard Karls University of Tübingen, Tübingen, Germany. [3]These authors contributed equally: Nicole Scholz, Anne-Kristin Dahse. ✉e-mail: scholzlab@gmail.com; tobias.langenhan@gmail.com

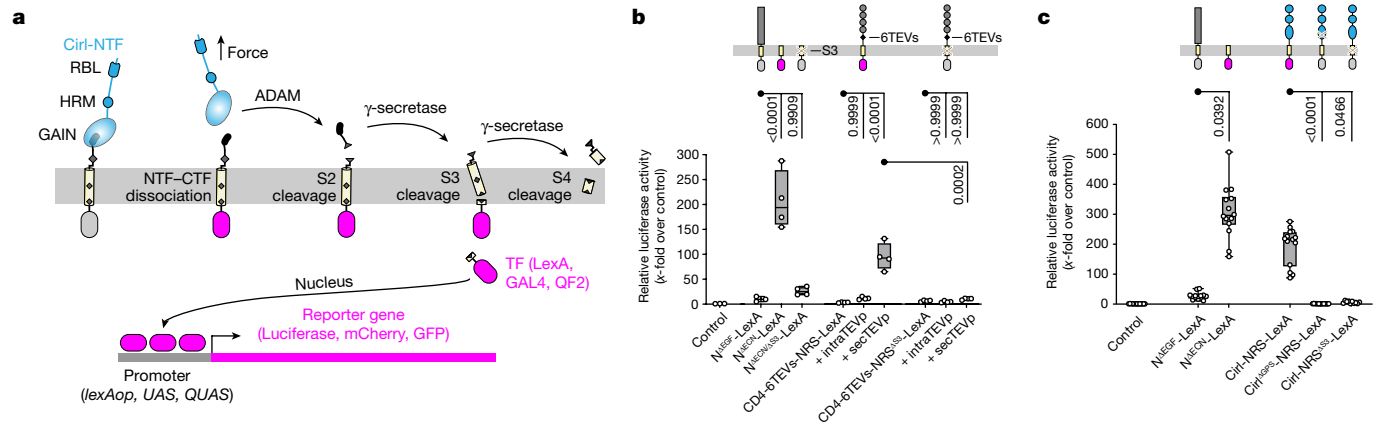

Fig. 1 | Activation of the NRS for the aGPCR Cirl depends on proteolysis of the GAIN domain. a, Exposure of Cirl or Cirl-NRS to its activating conditions (ligand and/or mechanical force) results in the separation of the Cirl heterodimer at the GPS, which allows for subsequent processing of the Notch JTS and release of the transcription factor (TF). In consequence, aGPCR dissociation is converted into the activation of a reporter or actuator transgene. HRM, hormone-receptor motif; RBL, rhamnose-binding lectin. **b**, Luciferase assay showing that the activation of $N^{\Delta ECN}$-LexA and CD4-6TEVs-NRS-LexA depends on γ-secretase substrate recognition, which is blocked by a crucial S3 site mutation in the JTS. Data ($n = 4$ biological replicates for all groups, except the control and $N^{\Delta EGF}$-LexA groups ($n = 3$) from one representative experiment) were normalized and presented as multiples of the control dataset in box-and-whisker plots (all data points plotted; horizontal line, median; boxes, 25th and 75th percentiles; whiskers, minimum and maximum values). Data were analysed with an ordinary one-way ANOVA with Tukey's test (confidence interval = 95%). *P* values are shown. See also Source Data. **c**, The Cirl-NRS-LexA sensor shows spontaneous activity in Schneider-2 cells, which is suppressed by abrogation of GAIN-domain autoproteolysis ($Cirl^{\Delta GPS}$-NRS-LexA) or γ-secretase cleavage (Cirl-$NRS^{\Delta S3}$-LexA). Data ($n = 14$ biological replicates for all groups, except the Cirl-$NRS^{\Delta S3}$-LexA group ($n = 10$) from three independent experiments) were normalized and presented as multiples of the control dataset in box-and-whisker plots as in **b** (all data points plotted). Data were analysed with a Kruskal–Wallis one-way ANOVA with Dunn's test (confidence interval = 95% for all comparisons). *P* values are shown. See also Source Data.

Delta or Serrate. Ligand endocytosis in *trans* transmits mechanical force onto the Notch ECR, which causes the exposure of a juxtamembrane receptor region[3,4,32] that is shielded by the negative regulatory region (NRR) during inactivity (Extended Data Fig. 2a). A juxtamembrane S2 site becomes accessible and is cleaved by an ADAM metalloprotease (for example, TACE or Kuzbanian)[31] outside the plasma membrane, leading to the shedding of most of the Notch ECR (Extended Data Fig. 2b). Successive regulated intramembrane proteolyses of the remaining Notch transmembrane fragment by the γ-secretase complex at S3 and S4 sites follow[33–35] (Extended Data Fig. 2b). The Notch intracellular domain (NICD) is finally released off the inner leaflet of the plasma membrane, enters the nucleus and co-activates the transcription of target genes (Extended Data Fig. 2b). We used the fly Notch juxta- and transmembrane segment (JTS), including the S2–S4 cleavage sites, to construct the NRS (Extended Data Figs. 1c and 2a,c), and replaced the NICD with the LexA-VP16 transcription factor to mark NRS activation through the LexA-*lexAop* binary expression system (Fig. 1a and Extended Data Fig. 1c). Previous work has shown that the Notch ECR, including the NRR, can be replaced by heterologous domains while still protecting the signal-initiating S2 site from protease engagement[36]. We confirmed this observation by fusing four immunoglobulin (Ig) domains of the human CD4 receptor N-terminally appended to the fly $Notch^{JTS}$, which inhibited the release of LexA in luciferase assays in *Drosophila* Schneider-2 cells to levels comparable to those of a constitutively inactive $Notch^{\Delta EGF}$ ($N^{\Delta EGF}$)–LexA control[35] (Extended Data Fig. 3a). Next, we inserted tri- or hexarepeats of the highly selective Tobacco etch virus (TEV) protease cleavage site (TEVs) between CD4-Ig repeats and $Notch^{JTS}$ (CD4-3TEVsNRS-LexA or CD4-6TEVs-NRS-LexA) for conditional separation of the ECR and $Notch^{JTS}$ of the sensor and exposure of the S2 site through TEV protease (TEVp). Co-expression of a secreted version of TEVp (secTEVp), but not its intracellular expression (intraTEVp) or when it was not expressed at all, led to strong activation of both the CD4-3TEVs-NRS-LexA and the CD4-6TEVs-NRS-LexA sensor in luciferase (Extended Data Fig. 3a) and fluorescent mCherry reporters (Extended Data Fig. 3b) in Schneider-2 cells, respectively. A constitutively active $N^{\Delta ECN}$-LexA (ref. [37]) served as a positive control (Extended Data Fig. 3a,b). Replacing a crucial valine residue with lysine at the S3 site[33] ($N^{\Delta ECN/\Delta S3}$-LexA) (Fig. 1b and Extended Data Fig. 3c) and pharmacological inhibition of γ-secretase activity with 10 µM DAPT abolished reporter activity (Extended Data Fig. 3d).

Next, we fused the complete ECR of the *Drosophila* ADGRL1–ADGRL3 (latrophilin) homologue, calcium-independent receptor of latrotoxin (Cirl) (containing all receptor components from the receptor N terminus to the beginning of the first transmembrane helix), to the NRS core sequence (Cirl-NRS-LexA; Extended Data Figs. 1c and 2c). Cirl-NRS-LexA readily showed high activity in Schneider-2 cells, indicating spontaneous dissociation of the NTF–CTF heterodimer under in vitro assay conditions, which exposed the S2 site (Fig. 1c). This was confirmed by replacement of a conserved histidine (−2 position) with alanine at the GPCR proteolysis site (GPS) of the sensor[10], which blocked GAIN-domain self-cleavage, eventual NTF release and NRS activity (Fig. 1c). Cirl-$NRS^{\Delta S3}$-LexA was also inactivated by the S3 site mutation (Fig. 1c). In enzyme-linked immunosorbent assays (ELISAs), only minor defects were observed in the cell-surface abundance of $Cirl^{\Delta GPS}$-NRS-LexA and Cirl-$NRS^{\Delta S3}$-LexA sensors (Extended Data Fig. 3e), which do not seem to account for the more severe reductions of reporter activities (Fig. 1c).

In vivo validation of Cirl-NRS

We generated minigenes for *Cirl-NRS-LexA*, *$Cirl^{\Delta GPS}$-NRS-LexA* and *Cirl-$NRS^{\Delta S3}$-LexA* using a *Drosophila* genomic engineering platform for *Cirl* (refs. [9,10]) that placed the transgenes under endogenous transcriptional control (Extended Data Fig. 4a). When activated, Cirl-NRS-LexA stimulates the expression of suitable reporter transgenes (Extended Data Fig. 5a–d). In adult flies, Cirl-NRS-LexA activity was detected in the eye, proboscis and leg joints (Extended Data Fig. 4b,e). To control for potential misexpression inherent to LexA, we also created *Cirl-NRS* transgenes that terminated in GAL4 or QF2 transcription-factor cassettes. Comparison of the activities of Cirl-NRS-LexA (Extended Data Fig. 4b,e), Cirl-NRS-GAL4 (Extended Data Fig. 4c,f) and Cirl-NRS-QF2 (Extended Data Fig. 4d,g) showed that all three sensors resulted in anatomically similar expression patterns. However, although the

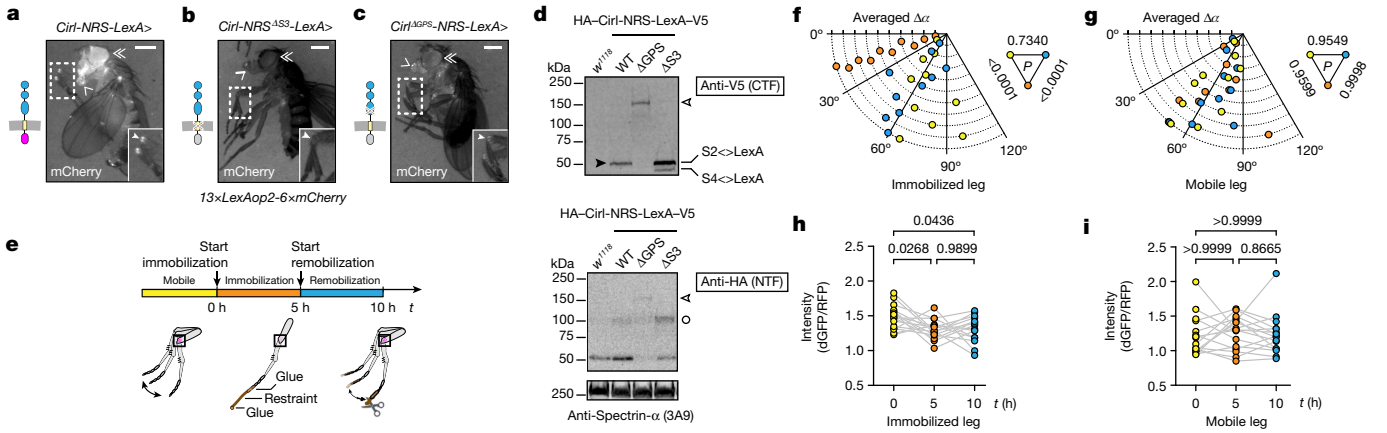

Fig. 2 | Cirl-NRS is activated in a mechano-dependent manner. a–c, Cirl-NRS-LexA activity (**a**) in the proboscis (chevron), eyes (double chevron) and leg joints (arrowheads) of adult flies is abrogated when γ-secretase (**b**) or GAIN-domain cleavage (**c**) is suppressed by point mutations, although residual signals are observed in the latter condition. Scale bars, 0.5 mm. **d**, Western blot of HA–Cirl-NRS-LexA–V5 variants as indicated above each lane blotted against an N-terminal HA tag and a C-terminal V5 tag. Cirl-NRS-LexA showed a C-terminal protein fragment (black arrowhead) representing the sensor protein after GAIN-domain cleavage. Weak bands corresponding to unprocessed full-length sensor protein (white arrowhead) and Cirl-NTF (white circle) are also visible. Inhibition of GAIN-domain cleavage (ΔGPS) yielded the full-length sensor protein (white arrowhead) and suppressed the generation of smaller fragments, indicating that proteolysis of the Notch^{JTS} component depends on GAIN proteolysis. Elimination of the γ-secretase cleavage site of the sensor (ΔS3) produced a double band indicating the C-terminal Cirl-NRS-LexA cleavage products of S2 and S4 proteolyses. A protein sample from w^{1118} flies served as a negative control; the loading control was performed with a Spectrin-α antiserum. The experiment was independently repeated twice with similar results. For gel source data, see Supplementary Fig. 1a–c. WT, wild type. **e**, Protocol for immobilization of the femorotibial joint. *t*, time. **f**,**g**, Joint angle range (Δα) of immobilized (**f**) and mobile (**g**) legs before (yellow), during (orange) and after (blue) immobilization. Data plotted on the same circle correspond to the averaged flexion–extension angle range of the same joint at the indicated time intervals. In each fly, one metathoracic leg was immobilized and the contralateral leg served as the mobile control ($n = 10$ independent flies per condition). Data groups were compared with a repeated-measures one-way ANOVA with Geisser–Greenhouse correction and Tukey's test (confidence interval = 95%). *P* values are shown in the triangle. See also Source Data. **h**,**i**, Cirl-NRS activity in femorotibial-joint neurons depends on the mechanical force produced by joint flexion ($n = 16$ independent flies per condition). Immobilized leg dataset groups were compared with a repeated-measures one-way ANOVA with Geisser–Greenhouse correction and Tukey's test; mobile leg dataset groups were analysed with the Friedman method and Dunn's multiple comparisons test (confidence interval = 95% for all comparisons). *P* values are shown. See also Source Data.

first two types of NRS showed comparable activities (Extended Data Fig. 4b,c,e,f), the Cirl-NRS-QF2 signal was considerably weaker in the legs and stronger in the eyes (Extended Data Fig. 4d,g).

Inhibition of S3 cleavage in the Cirl-NRS$^{\Delta S3}$-LexA reporter entirely abrogated sensor activity at all major expression sites (eye, leg joints and proboscis; Fig. 2a,b), confirming that Notch^{JTS} activity is absolutely necessary for NRS activity. Flies expressing the autoproteolysis-deficient Cirl$^{\Delta GPS}$-NRS-LexA sensor showed largely diminished reporter signals in all expression sites (Fig. 2c). Thus, abrogation of the NTF–CTF dissociation of Cirl-NRS-LexA, and therefore Cirl, is occurring in these tissues under physiological conditions.

Western blot analysis using a C-terminal V5 tag showed GPS cleavage of the wild-type Cirl-NRS-LexA sensor, indicating that the autoproteolytic activity of the GAIN domain was unimpeded in the chimeric sensor protein in flies in vivo (Fig. 2d). Blockade of GPS cleavage resulted in a single band corresponding to the full-length sensor protein (Fig. 2d). No smaller Cirl-NRS-LexA fragments derived from S2, S3 and S4 cleavages were observed, indicating that no regulated intramembrane proteolysis occurred in the absence of GAIN-domain cleavage (Fig. 2d). Western blotting of Cirl-NRS$^{\Delta S3}$-LexA confirmed that S3 proteolytic processing of Cirl-NRS-LexA is quenched by the V-to-K mutation (Fig. 2d). Altogether, these results show that Cirl-NRS-LexA activation is dependent on the self-cleavage of the GAIN domain, and that the chain of molecular events after NTF release within the NRS is unidirectional and sequentially unfolds in the intended order: NTF–CTF dissociation → S2 cleavage → S3 cleavage → LexA membrane release (Fig. 1a).

Mechanical forces stimulate Cirl-NRS

The release of the NTF after separation of the NTF–CTF receptor heterodimer suggests an obvious consequence of aGPCR mechanostimulation[15–17,22,26,38]. The activity of different mechanosensitive neuron classes in *Drosophila* depends on *Cirl* (refs. [9–11]). As the ECRs of the Cirl-NRS and Cirl proteins are identical (Extended Data Fig. 1a,c)—and, thus, exposed to similar adequate stimuli—we tested whether NTF release and the resulting Cirl-NRS activation depend on physiologically relevant mechanical stimuli. We focused on proprioceptive neurons in the adult leg joints, which are stretched and relaxed by joint motion[39]. These neurons are amenable to non-invasive mechanical manipulation, and exhibit high Cirl-NRS activity (Fig. 2a and Extended Data Fig. 4b–g) that requires Cirl autoproteolysis (Fig. 2c). To capture the dynamics of Cirl-NRS activity in the leg-joint neurons through its transcriptional output, we used a *UAS-TransTimer* transgene that simultaneously expresses a fast-folding destabilized GFP (dGFP) and a stable slow-folder long-lived RFP under Cirl-NRS-GAL4 control[40].

Adult flies expressing *Cirl-NRS-GAL4>UAS-TransTimer* were glued to a support to allow all legs to move freely for several hours, resulting in steady-state NTF release off the Cirl-NRS-GAL4 sensor through joint motion (Fig. 2e and Extended Data Fig. 6a; mobile interval). To stop joint bending and test the suppression of NTF release, we fixed one metathoracic leg in an extended position by gluing a taut restraint, made of a human hair, to its tarsus and the supporting plate to immobilize it (Fig. 2e and Extended Data Fig. 6b,c; immobilization interval). The contralateral metathoracic and all other legs remained mobile ($t = 0$ h). After the immobilization interval ($t = 5$ h), the fixed leg was released by cutting the hair and all legs were allowed to move for another 5 h ($t = 10$ h; Fig. 2e; remobilization interval). The range of motion (Extended Data Fig. 6d) of the immobilized femorotibial joint was significantly reduced and showed complete recovery thereafter (Fig. 2f), whereas the control leg exhibited high joint motion throughout the experiment (Fig. 2g). This indicated that joint immobilization could suppress the generation of mechanical force on mechanosensory

neurons, and that the fixed leg and the entire fly had remained intact and viable during the procedure.

At the end of each interval, we obtained dGFP/RFP values from the femorotibial-joint neurons of immobilized and mobile legs expressing *Cirl-NRS-GAL4>UAS-TransTimer*. The activity of Cirl-NRS-GAL4 was significantly reduced only in the immobilized leg neurons 5 h after fixation (Fig. 2h), whereas it showed sustained activity in the mobile control leg neurons (Fig. 2i), implying that Cirl-NRS activity is stimulated by mechanical force. Cirl-NRS-GAL4 activity in the immobilized joint neurons did not reach baseline values after remobilization (Fig. 2h), possibly owing to the longer time intervals required to re-establish steady-state sensor or reporter levels—which, however, were incompatible with fly viability.

Cirl-NRS activity in the larval brain

To map the disruption of the Cirl heterodimer at the cellular level, we turned to the nervous system of third instar (L3) larvae. Cirl-NRS-LexA^{+} cells were found throughout the ventral nerve cord (VNC) and central brain, highlighting the cell populations in which the release of Cirl-NTF is physiologically relevant (Extended Data Fig. 7a). In addition, suppression of regulated intramembrane S3 proteolysis (Cirl-NRS$^{\Delta S3}$-LexA) resulted in the complete loss of sensor activity (Extended Data Fig. 7b). Notably, abolition of GAIN-domain self-cleavage caused the loss of Cirl$^{\Delta GPS}$-NRS-LexA activity in most of the central nervous system (CNS) except the mushroom body (Extended Data Fig. 7c), perhaps through the expression of a specific set of enzymes (for example, sheddases) that catalyse additional or alternative proteolytic processing of Cirl or Cirl-NRS-LexA (ref. [41]). Thus, the NRS system may be suitable for reporting additional cleavage events at aGPCR ECRs as well.

Immunohistochemical detection of the N and C termini of Cirl-NRS proteins in L3 brains through confocal imaging showed that the wild-type, ΔS3 and ΔGPS (Extended Data Fig. 7j–l) variants were indistinguishably colocalized at the membrane of expressing cells (Extended Data Fig. 7d–i).

Flies co-expressing Cirlp-GAL4^{+} (ref. [9]) and Cirl-NRS-LexA^{+} reporters showed signals throughout the VNC and brain hemispheres of the L3 CNS (Extended Data Fig. 7a,m). To ensure that the subcellular localization of Cirl-NRS-LexA and Cirl corresponded, we examined their expression pattern in flies co-expressing an RFP-Cirl fusion protein[10] and the Cirl-NRS-LexA sensor variants' V5 tag. Inspection of co-stainings of larval brain hemispheres showed that RFP-Cirl and Cirl-NRS-LexA were colocalized at cell boundaries (Extended Data Fig. 7n), irrespective of whether proteolytic processing was disabled at the S3 (Cirl-NRS$^{\Delta S3}$-LexA; Extended Data Fig. 7o) or GPS (Cirl$^{\Delta GPS}$-NRS-LexA; Extended Data Fig. 7p) sites.

Cirl-NTF release requires Tollo

If Cirl receptor dissociation occurs after the transmission of mechanical force through ligands, ligand removal should curtail Cirl-NRS activation. We identified Cirl ligands through an affinity-immunoprecipitation screen using RFP-Cirl (ref. [10]) as bait. Pupal lysates were collected and RFP-Cirl was pulled down using magnetic beads pre-adsorbed with a polyclonal anti-RFP antiserum (Extended Data Fig. 8a). Mass spectrometry analysis identified and quantified around 1,100 proteins through label-free quantification (LFQ) of the $\log_2$-transformed fold change between RFP-Cirl and a RFP-fused synaptobrevin (Syb) control bait to exclude unspecific binders. We identified 90 proteins that were potential Cirl interactors. Tollo (also known as Toll-8 and CG6890) was identified as a candidate ligand and was quantified using a total of 4 unique peptides and a confidence *P* value of 4.8×10^{-153} (Fig. 3a). Previous work identified Tollo as a ligand of Cirl in the *Drosophila* embryo[12] by using a ligand screening set-up (bait: overexpressed Tollo) inverse to ours (bait: endogenously expressed Cirl). This supported the utility of Tollo as a reliable tool to demonstrate the NTF–CTF dissociation of Cirl in vivo.

We searched for the apposition of Cirl^{+} and Tollo^{+} cells by co-expression of *Cirl-NRS-LexA* and *Tollo-GAL4*, a reporter of transcriptional activity of the *Tollo* gene (Fig. 3b,c and Extended Data Fig. 8b). To identify sites of potential cell–cell contact, we used a membrane-bound *lexAop-myr::mCherry* reporter and a *UAS-6×GFP* transgene producing a cytoplasmic fluorophore. Similar to its expression sites in the adult CNS, *Tollo-GAL4* showed abundant expression in L3 brains, marking clusters of secondary neuron lineages and their axon tracts[42] (Fig. 3b,c), whereas the *Cirl-NRS-LexA* signal was most prominent in mushroom-body neurons and their projections in the VNC (Extended Data Fig. 8b), consistent with the expression pattern documented for the Cirl-NRS-LexA sensor protein (Fig. 3f and Extended Data Fig. 7a).

To corroborate the apposition of *Cirl-NRS-LexA*$^{+}$ and *Tollo-GAL4*$^{+}$ cells, we used the t-GRASP (targeted GFP reconstitution across synaptic partners) technique[43,44] (Extended Data Fig. 8c). We used cacophony (Cac::GFP11) as the presynaptic (pre-t-GRASP) and telencephalin (TLN::GFP1-10) as the postsynaptic (post-t-GRASP) partner protein. Each component is non-fluorescent and non-immunogenic on its own. Only when both fragments reconstitute GFP, upon contact, can they be detected with a monoclonal anti-GFP antibody[43]. When we co-expressed *Tollo-GAL4>pre-t-GRASP* and *Cirl-NRS-LexA>post-t-GRASP*, we observed discrete GFP immunosignals throughout the central brain lobes (Extended Data Fig. 8e), whereas omission of the driver transgenes significantly reduced t-GRASP signals (Extended Data Fig. 8d). Quantification of the t-GRASP profiles confirmed that Cirl-NRS-LexA is activated in cells that contact *Tollo*$^{+}$ neurons (Extended Data Fig. 8f).

The activity of Cirl-NRS-LexA in adults and L3 larvae (Fig. 3d–i) was abrogated by genetic removal of *Tollo* (Fig. 3h,i). Notably, strong Cirl-NRS-LexA signals in the adult eye, brain and leg-joint neurons (Fig. 3e,f) were lost in a *Tollo^{CS}/Df(3L)BSC578* background (Fig. 3h). In addition, the activity of Cirl-NRS-LexA was suppressed in the larval central brain, mushroom body and VNC; only a few cells showed background signals (Fig. 3i). Notably, expression of full-length Cirl–V5 in adult heads and larval brains seemed to be unaffected by the loss of *Tollo* when analysed in western blots and immunostaining (Extended Data Fig. 8g–i). These results show that the activation of Cirl-NRS-LexA requires Cirl's ligand, Tollo.

Cirl and Tollo interact in *cis* and in *trans*

Apart from neuronal profiles in the VNC and mushroom body, examination of Cirl-NRS-LexA expression revealed a reticular pattern in the central brain (Figs. 3b,c and 4a,c). This arrangement is reminiscent of the trophospongium chambers that are established by the lamellipodia of cortex glial (CG) cells, in which neuroblasts, ganglion mother cells (GMCs) and their secondary lineage progeny are enveloped in the late larval brain[45]. Although thus far *Cirl* has been regarded as a neuron-specific gene[9–11], glial Cirl-NRS activity was confirmed by colocalization with the CG-cell-specific *55B12-GAL4* driver (Fig. 4a,c) and in a subset of cells expressing the pan-glial *repo-GAL4* marker in the cortex (Extended Data Fig. 9a).

Individual neuroblasts, GMCs, their daughter lineages and axon tract bundles express *Tollo-GAL4* (Fig. 3b,c and 4c), whereas *Cirl-NRS-LexA*$^{+}$ CG cells enwrap each lineage nest and show *Cirl-NRS-LexA*$^{+}$ activation (Fig. 4a,c). We constructed a *Cirl-T2A-LexA* reporter, which leads to the co-translational production of LexA along with the *Cirl* gene product through ribosomal skipping, thereby indicating Cirl protein synthesis (Extended Data Fig. 9b). This reporter shows that *Cirl* is also expressed in the neuroblast lineage (Fig. 4b). In sum, Tollo is only produced in neurons of the CG-cell–neuroblast lineage interface, whereas Cirl is expressed on both the glial and the neuronal side. As Cirl-NRS-LexA activation only occurs in CG cells but not in the anti-Mir^{+} (Miranda) neuroblast lineage, Tollo and Cirl engage in *trans* at the CG-cell–neuroblast boundary (Figs. 3b,c and 4c,d and Extended Data Fig. 8d–f) to cause Cirl dissociation on CG cells (Fig. 4a,e,f; *trans*-activation of

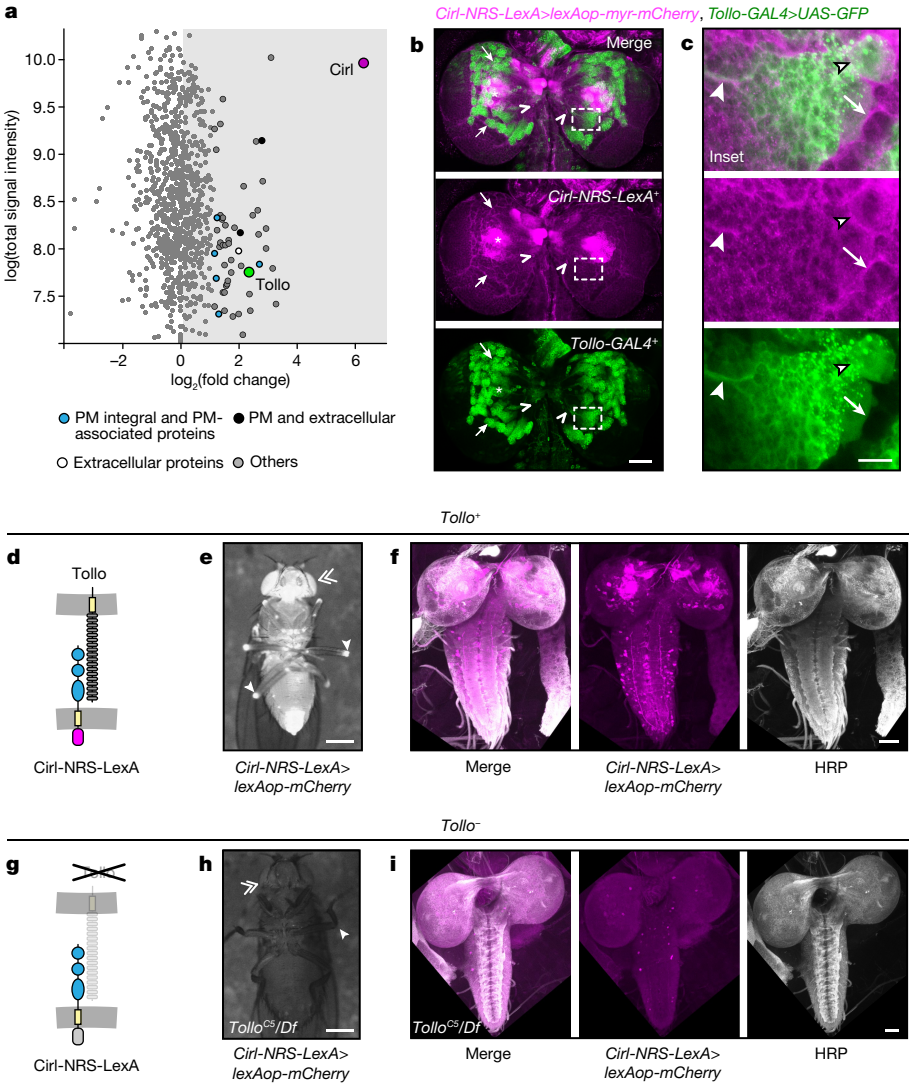

Fig. 3 | Cirl receptor dissociation requires interaction with its ligand Tollo. **a**, Mass spectrometry analysis reveals putative binding partners of Cirl. The results are shown as a scatter plot according to their LFQ $\log_2$ ratio against the control bait (*x* axis) and $\log_{10}$ of total protein intensity (*y* axis). Putative interactors of Cirl were identified using a one-sided significance A statistical test (outliers, one-sided *Q*-test with a *P* value < 0.05), and are highlighted according to their subcellular localization. PM, plasma membrane. **b**, *Tollo-GAL4* and *Cirl-NRS-LexA* co-labelling shows discrete sites of *Cirl-NRS-LexA*$^+$ (magenta) and *Tollo-GAL4*$^+$ (green) proximity in brain hemispheres. Strong *Cirl-NRS-LexA>lexAop-myr-mCherry* activity in the central brain is found in the mushroom body (MB) (asterisk), in a reticular pattern in the cortex (arrows) and in neuron-like cells (chevrons). Scale bars, 50 µm. The experiment was independently repeated six times with similar results. **c**, Insets of **b** show reticular *Cirl-NRS-LexA*$^+$ label (arrows) surrounding a *Tollo-GAL4*$^+$-labelled cell nest (neuroblasts indicated by black-outlined arrows). *Tollo-GAL4*$^+$ signals are present in the axon bundle tract (white arrowheads). Scale bars, 10 µm. The experiment was independently repeated six times with similar results. **d**, Cirl-NRS-LexA and Tollo configuration in wild-type flies. **e**, Wild-type adult flies show abundant Cirl-NRS-LexA activity in the eye (double chevron) and leg joints (arrowheads) (NRS signal$^+$: 84/84 independent flies inspected). The experiment was independently repeated six times with similar results. Scale bar, 0.5 mm. **f**, Wild-type L3 larvae with Cirl-NRS-LexA activation pattern in the CNS. Scale bar, 50 µm. The experiment was independently repeated six times with similar results. **g**, Cirl-NRS-LexA configuration in Tollo-deficient (*Tollo*^{CS}*/Df*) flies. **h**,**i**, Genetic removal of *Tollo* suppresses Cirl-NRS-LexA activation in adults (**h**; NRS signal$^+$: 8/120 individual flies inspected) and larvae (**i**; NRS signal$^+$: 0/8 individual flies inspected). HRP, α-horseradish peroxidase antiserum. Scale bars, 0.5 mm (**h**) and 50 µm (**i**).

Cirl-NRS-LexA). The loss of Cirl-NRS-LexA activity that is observed in CG cells of *Tollo*^{KO} mutants supports this conclusion (Fig. 3g–i).

We overexpressed a *Tollo-YFP* transgene ectopically in CG cells by using the *55B12-GAL4* driver to place Tollo in *trans* to Cirl in neuroblasts and GMCs, thereby inverting the physiological expression pattern of Tollo at the CG-cell–neuroblast boundary (Fig. 4e–g). This caused the activation of Cirl-NRS-LexA in the neuroblast lineage (Fig. 4g) confirming the *trans*-activity of Tollo on Cirl-NRS-LexA dissociation. Of note, ectopically expressed Tollo suppresses Cirl-NRS in CG cells in *cis* (Fig. 4g), and bypasses the endogenous activation of Cirl-NRS in CG cells through Tollo expressed by neuroblasts in *trans*. This indicates that co-expression of Cirl and Tollo in *cis* inhibits the release of Cirl-NTF (Fig. 4e–g; *cis*-inhibition of Cirl-NRS-LexA). We tested whether this *cis* interaction and lack thereof accounted for the high Cirl-NRS-LexA activity in Schneider-2 cells (Fig. 1c). When co-expressed with the Cirl-NRS-LexA reporter, increasing amounts of Tollo gradually suppressed NRS activation to background levels, but had no effect on a Cirl-NRS$^{\Delta S3}$-LexA control reporter (Fig. 4h). This supports the model that *cis*-Tollo suppresses Cirl dissociation.

Cirl-NTF release regulates the number of neuroblasts

Genetic removal of *Cirl* significantly increased the number of anti-Mir$^+$ neuroblasts in L3 central brains (Fig. 4i,j), suggesting that Cirl has a

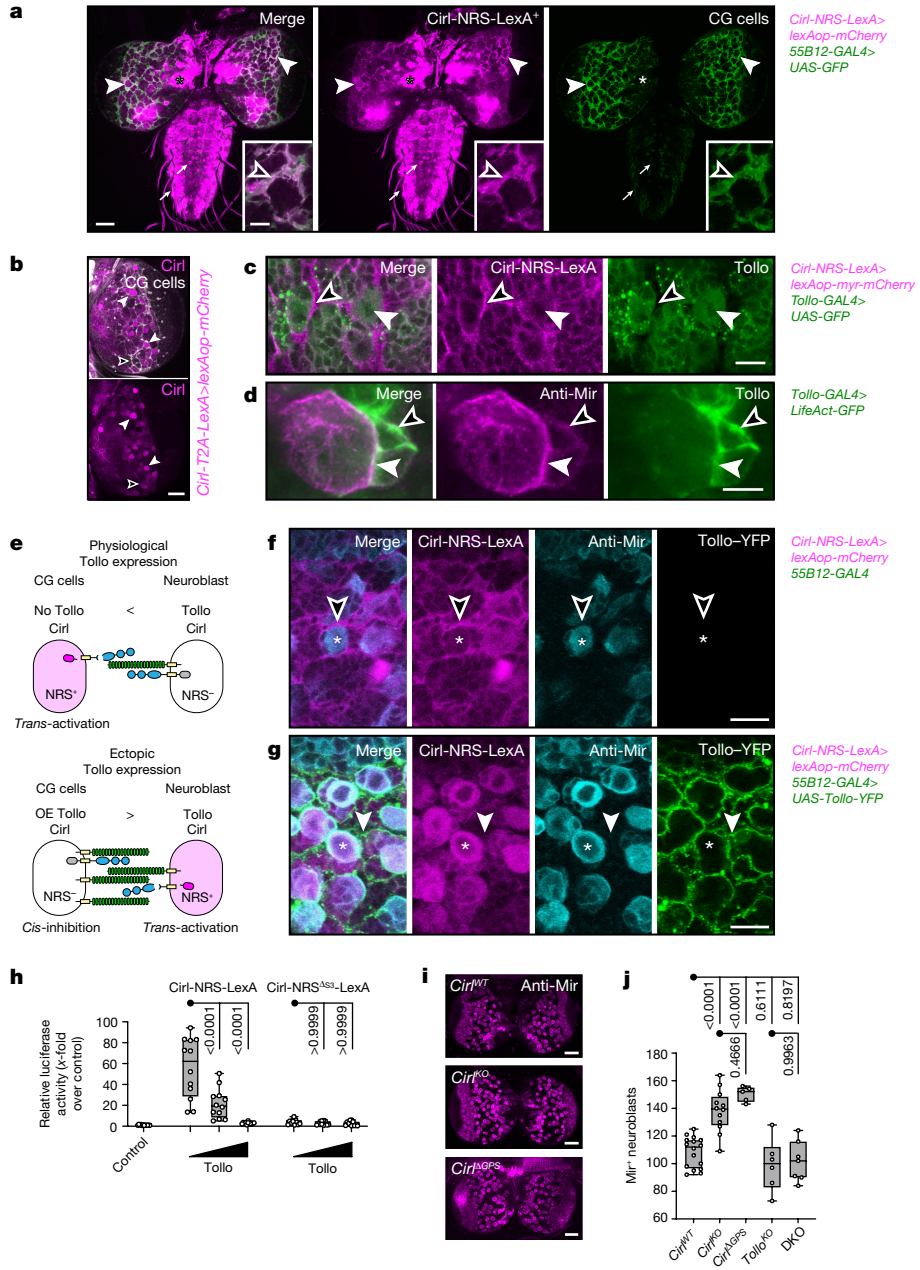

Fig. 4 | Cirl-NTF dissociates at CG cells to regulate the pool of neuroblasts. **a**, Cirl dissociation occurs in the mushroom body (asterisk), VNC neurons (arrows) and CG cells (closed arrowheads). Confocal plane showing co-expression of *Cirl-NRS-LexA* and the CG-cell-specific *GMR55B12-GAL4*. Scale bar, 50 µm. Inset, lamellipodia of CG cells (open arrowheads). Scale bar, 10 µm. The experiment was independently repeated six times with similar results. **b**, *Cirl-T2A-LexA* expression in neuroblasts. White arrowheads, neuroblasts; black arrowheads, CG cells visualized by *Kr-GAL4>UAS-GFP*. Scale bar, 10 µm. The experiment was independently repeated six times with similar results. **c**, CG cells lack Tollo expression. Neuroblasts (white arrowheads) and CG cells (black arrowheads). Scale bar, 50 µm. The experiment was independently repeated six times with similar results. **d**, Tollo is expressed in neuroblasts, GMCs and neurons (black arrowheads). Neuroblasts (white arrowheads) visualized by anti-Mir staining. Scale bar, 5 µm. The experiment was independently repeated six times with similar results. **e**, Cirl–Tollo interaction experiments at the CG-cell–neuroblast lineage interface. OE, overexpression. **f**, Cirl and Tollo expression in neighbouring cells activates Cirl-NRS-LexA in CG cells (*trans*-activation; magenta; black arrowhead), whereas neuroblasts (turquoise) show no Cirl-NRS-LexA activity (asterisk). Scale bar, 15 µm. The experiment was independently repeated six times with similar results. **g**, Cirl-NRS-LexA activity in CG cells is suppressed by ectopic overexpression of Tollo-YFP (green) in CG cells (*cis*-inhibition; white arrowhead) and activated in neuroblasts (*trans*-activation; magenta; asterisk). Neuroblasts, anti-Mir. Scale bar, 15 µm. The experiment was independently repeated six times with similar results. **h**, Tollo *cis*-expression suppresses Cirl-NRS-LexA activity in Schneider-2 cells, whereas Cirl-NRS$^{\Delta S3}$-LexA is not affected. Data ($n = 12$ biological replicates from three independent experiments for all groups) were normalized and presented as multiples of the control dataset in box-and-whisker plots (all data points plotted; box-plot parameters as in Fig. 1b). Data were analysed with an ordinary one-way ANOVA with Tukey's test (confidence interval = 95% for both comparisons). *P* values are shown. See also Source Data. **i**, The number of anti-Mir$^+$ neuroblasts (magenta) is increased in *Cirl*^{KO} and *Cirl*$^{\Delta GPS}$ mutants. Scale bars, 50 µm. **j**, Removal of *Tollo* curtails the *Cirl*^{KO}-associated increase of neuroblasts in *Cirl*^{KO};*Tollo*^{KO} double-knockout (DKO) flies. anti-Mir$^+$ neuroblast counts in the central brain in *Cirl*^{WT} ($n = 16$), *Cirl*^{KO} ($n = 12$), *Cirl*$^{\Delta GPS}$ ($n = 5$), *Tollo*^{KO} ($n = 6$) and *Cirl*^{KO};*Tollo*^{KO} DKO mutants ($n = 7$). Data are presented in a box-and-whisker plot (all data points plotted; box-plot parameters as in Fig. 1b). Data were analysed with an ordinary one-way ANOVA with Tukey's test (confidence interval = 95%). *P* values are shown. See also Source Data.

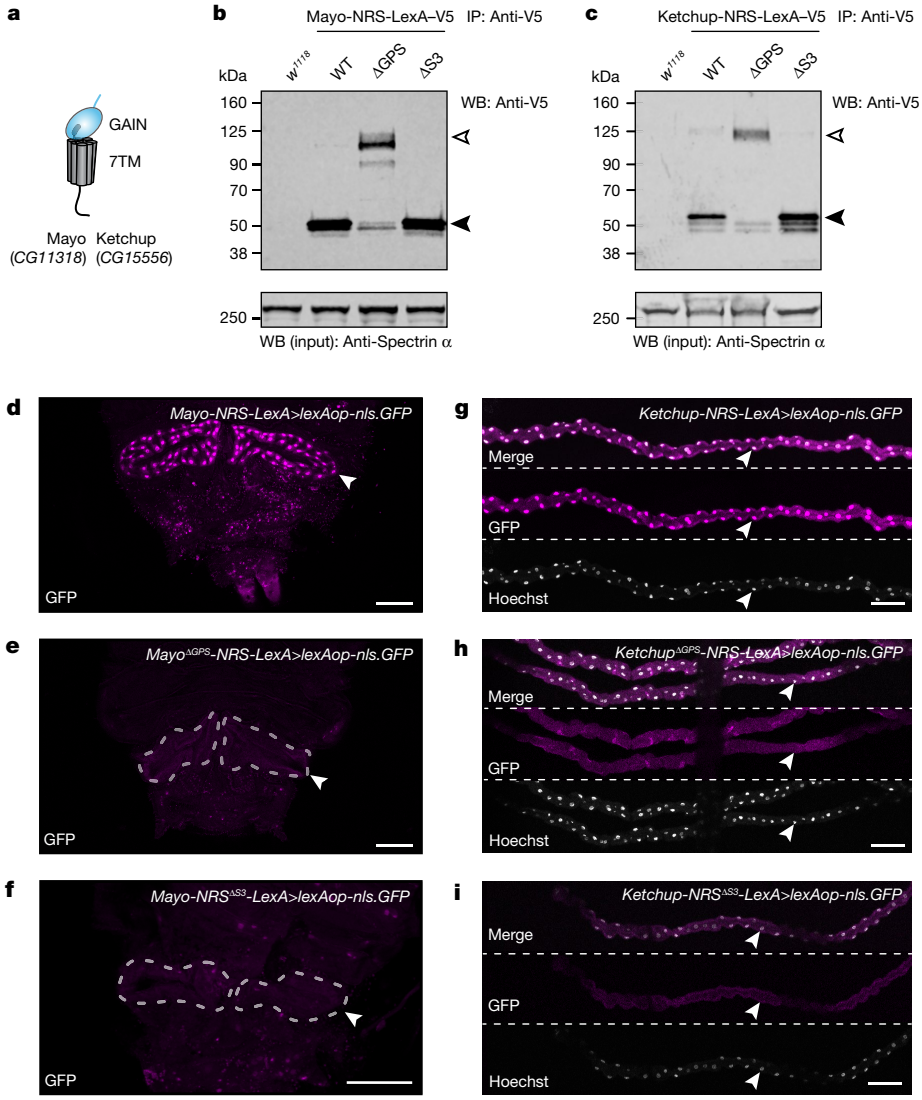

Fig. 5 | NRS for non-neural aGPCRs. a, Structure of Mayo-NRS and Ketchup-NRS. **b**,**c**, Western blots (WBs) of anti-V5 immunoprecipitated (IP) Mayo-NRS-LexA–V5 (**b**) and Ketchup-NRS-LexA–V5 (**c**) variants as indicated above each lane, blotted against a C-terminal V5 tag. GAIN-domain cleavage results in CTF bands of sensor proteins (black arrowheads). Inhibition of GAIN-domain cleavage (ΔGPS) yields full-length sensor proteins for both receptors (white arrowheads). Protein samples from w^{1118} flies served as a negative control; protein input samples immunoblotted with a Spectrin-α antiserum were used as loading controls. The experiment was independently repeated twice with similar results. For gel source data, see Supplementary Fig. 1d–g. **d**, Anal pad (arrowhead) of an L3 larva, showing Mayo-NRS-LexA activity. **e**,**f**, Abrogation of GPS (**e**) and γ-secretase (**f**) cleavage suppresses Mayo-NRS activity. Location of anal pads indicated by dashed outline. Scale bars, 150 µm. The experiment was independently repeated six times with similar results. **g**, Malpighian tubules (arrowheads) of an L3 larva, showing Ketchup-NRS-LexA activity. **h**,**i**, Abrogation of GPS (**h**) and γ-secretase (**i**) cleavage abrogates Ketchup-NRS activity. Hoechst counterstain in white. Scale bars,100 µm. The contrast and brightness were digitally increased in **e**,**f**,**h**,**i** to outline organs. The experiment was independently repeated six times with similar results.

role in neurogenesis. Notably, $Cirl^{\Delta GPS}$ mutant larvae containing an autoproteolysis-deficient *Cirl* allele showed a similarly expanded neuroblast population (Fig. 4i,j), whereas *Cirl-NRS-LexA/*$Cirl^{KO}$ larvae expressing only a releasable wild-type Cirl-NTF but no Cirl-CTF have normal numbers of neuroblasts (Extended Data Fig. 9c). Knockdown of *Cirl* expression through cell-specific RNA interference in either CG cells or neuroblasts and GMCs through *55B12-GAL4* or *Tollo-GAL4*, respectively, showed that *Cirl* is only required in CG cells but not in neuroblasts to maintain the neuroblast pool size (Extended Data Fig. 9d). Collectively, this suggests that the release of Cirl-NTF from CG cells non-cell-autonomously regulates the number of neuroblasts in the larval brain through engagement with Tollo on neuroblasts and GMCs. It also suggests that Cirl and Tollo interact in the same pathway as ligand and receptor, respectively, and that *Tollo* should thus be epistatic to *Cirl*. The numbers of neuroblasts in $Tollo^{KO}$ mutants are similar to those of wild-type controls, and removal of *Tollo* from the $Cirl^{KO}$ background (double knockout) rescues the increase in neuroblasts that was found in $Cirl^{KO}$ mutants, confirming this model (Fig. 4j). Together, these data show that at the CG-cell–neuroblast/GMC interface, released Cirl-NTF acts as a Tollo ligand to suppress the Tollo-dependent expansion of the pool of neuroblasts. aGPCR autoproteolysis allows this non-cell-autonomous function.

NRS for non-neural aGPCRs

Finally, we tested the universality of the NRS approach by recording the NTF release of other aGPCRs. Apart from *Cirl* and *Flamingo*(*Fmi*; also known as *Starry night* (*Stan*))[9,46], *Drosophila* contains three other

aGPCR genes[47,48]: *CG11318*, *CG15556* and *CG15744*, which we named *Mayo*, *Ketchup* and *Remoulade*, respectively (Extended Data Fig. 10a). *Mayo* and *Ketchup* encode receptors with a simple layout containing only the GAIN and 7TM domains (Fig. 5a). Bioinformatic evaluation of the GAIN-domain phylogeny confirms their placement in a separate primordial aGPCR subfamily (Extended Data Fig. 10b). *Remoulade* encodes an aGPCR with a typical subfamily A domain layout[14] (Extended Data Fig. 10a).

We inspected the GPS sequence of Mayo, Ketchup and Remoulade (Extended Data Fig. 10c). As Remoulade does not contain a canonical $H^{-2}L/I^{-1}T/S^{+1}$ motif[5], it was discarded from further analysis. We constructed Mayo-NRS-LexA and Ketchup-NRS-LexA versions (Extended Data Fig. 10d) by CRISPR–Cas9-mediated gene targeting of each gene following the same strategy as for *Cirl* (refs. [9,48]) (Extended Data Fig. 4a), generating sets of three transgenic fly stocks per aGPCR (NRS-WT, NRS-ΔGPS and NRS-ΔS3). Western blot analyses of immunoprecipitated pupal lysates in all NRS protein versions for Mayo (Fig. 5b) and Ketchup (Fig. 5c) showed that they are readily expressed in transgenic flies. Suppression of GPS cleavage in both NRS versions indicated that Mayo and Ketchup undergo GAIN-mediated autoproteolysis, and that NTF release activity can therefore principally be reported by Mayo-NRS and Ketchup-NRS. *Mayo* is endogenously expressed in the gut and anal pads, whereas *Ketchup* is found in the proventriculus and Malpighian tubules of L3 larvae as previously shown[48]. Mayo-NRS-LexA activity was observed throughout the anal-pad epithelium (Fig. 5d; 6 out of 6 flies). Suppression of GAIN-domain cleavage (ΔGPS; Fig. 5e) or γ-secretase cleavage (ΔS3; Fig. 5f) suppressed sensor activity (0 out of 6 analysed flies of each genotype showed NRS signals), providing evidence of its specificity to NTF release reported through the NRS. Similarly, Ketchup-NRS-LexA was activated in Malpighian tubule cells as visualized with a nuclear nls.GFP reporter and Hoechst counterstain (6 out of 6 flies), whereas ΔGPS and ΔS3 abrogated Ketchup-NRS activity (Fig. 5g–i; 0 out of 6 analysed flies of each genotype showed NRS signals). We conclude that the NRS system is applicable to other non-ADGRL-type and non-neural aGPCRs and offers a resource for investigating their biochemical processing, heterodimer dissociation and functional tasks in *Drosophila* and other experimental models.

Discussion

Mechanical activation has been noted for several aGPCRs[9,15,17,18], and offers a logical mechanism for NTF removal and TA uncapping. The NRS system that we introduce here uses the signal-transductive JTS core of Notch, which is a mechano-activated surface receptor in its own right[2–4]. We have used Notch proteolysis and generated artificial chimeric aGPCR–Notch–transcription-factor sensors to study spontaneous and ligand-induced NTF release from individual cells in culture and in an animal model. The NRS system allowed us to study non-cell-autonomous activities of latrophilin (Cirl) in the brain. Such non-cell autonomy of aGPCR functions is likely to contribute to the high evolutionary conservation of aGPCR autoproteolysis as a prerequisite for NTF release[6,15,16,22,26].

Cirl-NTF release is mediated by *trans*-Tollo, whereas *cis*-Tollo suppresses it. Whether Cirl-NTF dependent Tollo regulation feeds into known signalling outlets of Toll-like receptors[49] remains to be determined. Furthermore, the *cis*- and *trans*-engagement of Cirl–Tollo is reminiscent of Notch–Delta interactions, in which *cis*-stabilization and *trans*-activation flip Notch activity in an ultrasensitive manner[50].

NRS-based approaches will further our knowledge of the physiological roles of this receptor family, and their effects on disease processes. Because of its generic format, the NRS tool can accommodate any aGPCR layout, including human homologues. Thus, we foresee that the NRS system will facilitate the discovery and characterization of signalling conditions of individual aGPCRs, such as effects on ligand engagement, stimulation with adequate mechanical forces and non-GPS-cleavage steps. Moreover, the NRS system allows for the analysis of signalling modes that rely on aGPCR dissociation, and for the identification of compounds that modulate them. NRS-based drug screening will provide new avenues for the de-orphanization of aGPCRs and drug target discovery[13].

Online content

Any methods, additional references, Nature Portfolio reporting summaries, source data, extended data, supplementary information, acknowledgements, peer review information; details of author contributions and competing interests; and statements of data and code availability are available at https://doi.org/10.1038/s41586-023-05802-5.

1. Nieberler, M., Kittel, R. J., Petrenko, A. G., Lin, H.-H. & Langenhan, T. in *Adhesion G Protein-coupled Receptors: Molecular, Physiological and Pharmacological Principles in Health and Disease* (eds Langenhan, T. & Schöneberg, T.) 83–109 (2016).
2. Gordon, W. R. et al. Mechanical allostery: evidence for a force requirement in the proteolytic activation of Notch. *Dev. Cell* **33**, 729–736 (2015).
3. Meloty-Kapella, L., Shergill, B., Kuon, J., Botvinick, E. & Weinmaster, G. Notch ligand endocytosis generates mechanical pulling force dependent on dynamin, epsins, and actin. *Dev. Cell* **22**, 1299–1312 (2012).
4. Langridge, P. D. & Struhl, G. Epsin-dependent ligand endocytosis activates Notch by force. *Cell* **171**, 1383–1396 (2017).
5. Lin, H.-H. et al. Autocatalytic cleavage of the EMR2 receptor occurs at a conserved G protein-coupled receptor proteolytic site motif. *J. Biol. Chem.* **279**, 31823–31832 (2004).
6. Araç, D. et al. A novel evolutionarily conserved domain of cell-adhesion GPCRs mediates autoproteolysis. *EMBO J.* **31**, 1364–1378 (2012).
7. Krasnoperov, V. G. et al. α-Latrotoxin stimulates exocytosis by the interaction with a neuronal G-protein-coupled receptor. *Neuron* **18**, 925–937 (1997).
8. Gray, J. X. et al. CD97 is a processed, seven-transmembrane, heterodimeric receptor associated with inflammation. *J. Immunol.* **157**, 5438–5447 (1996).
9. Scholz, N. et al. The adhesion GPCR latrophilin/CIRL shapes mechanosensation. *Cell Rep.* **11**, 866–874 (2015).
10. Scholz, N. et al. Mechano-dependent signaling by latrophilin/CIRL quenches cAMP in proprioceptive neurons. *eLife* **6**, e28360 (2017).
11. Dannhäuser, S. et al. Antinociceptive modulation by the adhesion GPCR CIRL promotes mechanosensory signal discrimination. *eLife* **9**, e56738 (2020).
12. Lavalou, J. et al. Formation of polarized contractile interfaces by self-organized Toll-8/Cirl GPCR asymmetry. *Dev. Cell* **56**, 1574–1588 (2021).
13. Bassilana, F., Nash, M. & Ludwig, M.-G. Adhesion G protein-coupled receptors: opportunities for drug discovery. *Nat. Rev. Drug Discov.* **18**, 869–884 (2019).
14. Hamann, J. et al. International Union of Basic and Clinical Pharmacology. XCIV. Adhesion G protein-coupled receptors. *Pharmacol. Rev.* **67**, 338–367 (2015).
15. Yeung, J. et al. GPR56/ADGRG1 is a platelet collagen-responsive GPCR and hemostatic sensor of shear force. *Proc. Natl Acad. Sci. USA* **117**, 28275–28286 (2020).
16. Boyden, S. E. et al. Vibratory urticaria associated with a missense variant in *ADGRE2*. *N. Engl. J. Med.* **374**, 656–663 (2016).
17. Liu, D. et al. CD97 promotes spleen dendritic cell homeostasis through the mechanosensing of red blood cells. *Science* **375**, eabi5965 (2022).
18. Petersen, S. C. et al. The adhesion GPCR GPR126 has distinct, domain-dependent functions in Schwann cell development mediated by interaction with Laminin-211. *Neuron* **85**, 755–769 (2015).
19. Scholz, N., Monk, K. R., Kittel, R. J. & Langenhan, T. in *Adhesion G Protein-coupled Receptors: Molecular, Physiological and Pharmacological Principles in Health and Disease* (eds Langenhan, T. & Schöneberg, T.) 221–247 (2016).
20. Vizurraga, A., Adhikari, R., Yeung, J., Yu, M. & Tall, G. G. Mechanisms of adhesion G protein-coupled receptor activation. *J. Biol. Chem.* **295**, 14065–14083 (2020).
21. Beliu, G. et al. Tethered agonist exposure in intact adhesion/class B2 GPCRs through intrinsic structural flexibility of the GAIN domain. *Mol. Cell* **81**, 905–921 (2021).
22. Stoveken, H. M., Hajduczok, A. G., Xu, L. & Tall, G. G. Adhesion G protein-coupled receptors are activated by exposure of a cryptic tethered agonist. *Proc. Natl Acad. Sci. USA* **112**, 6194–6199 (2015).
23. Liebscher, I. et al. A tethered agonist within the ectodomain activates the adhesion g protein-coupled receptors GPR126 and GPR133. *Cell Rep.* **9**, 2018–2026 (2014).
24. Bohnekamp, J. & Schöneberg, T. Cell adhesion receptor GPR133 couples to G_s protein. *J. Biol. Chem.* **286**, 41912–41916 (2011).
25. Sando, R., Jiang, X. & Südhof, T. C. Latrophilin GPCRs direct synapse specificity by coincident binding of FLRTs and teneurins. *Science* **363**, eaav7969 (2019).
26. Frenster, J. D. et al. Functional impact of intramolecular cleavage and dissociation of adhesion G protein–coupled receptor GPR133 (ADGRD1) on canonical signaling. *J. Biol. Chem.* **296**, 100798 (2021).
27. Qu, X. et al. Structural basis of tethered agonism of the adhesion GPCRs ADGRD1 and ADGRF1. *Nature* **604**, 779–785 (2022).
28. Barros-Álvarez, X. et al. The tethered peptide activation mechanism of adhesion GPCRs. *Nature* **604**, 757–762 (2022).
29. Xiao, P. et al. Tethered peptide activation mechanism of the adhesion GPCRs ADGRG2 and ADGRG4. *Nature* **604**, 771–778 (2022).
30. Ping, Y.-Q. et al. Structural basis for the tethered peptide activation of adhesion GPCRs. *Nature* **604**, 763–770 (2022).

31. Kopan, R. & Ilagan, Ma. X. G. The canonical Notch signaling pathway: unfolding the activation mechanism. *Cell* **137**, 216–233 (2009).
32. Stephenson, N. L. & Avis, J. M. Direct observation of proteolytic cleavage at the S2 site upon forced unfolding of the Notch negative regulatory region. *Proc. Natl Acad. Sci. USA* **109**, E2757–E2765 (2012).
33. Schroeter, E. H., Kisslinger, J. A. & Kopan, R. Notch-1 signalling requires ligand-induced proteolytic release of intracellular domain. *Nature* **393**, 382–386 (1998).
34. Strooper, B. D. et al. A presenilin-1-dependent γ-secretase-like protease mediates release of Notch intracellular domain. *Nature* **398**, 518–522 (1999).
35. Struhl, G. & Adachi, A. Nuclear access and action of Notch in vivo. *Cell* **93**, 649–660 (1998).
36. Mumm, J. S. et al. A ligand-induced extracellular cleavage regulates γ-secretase-like proteolytic activation of Notch1. *Mol. Cell* **5**, 197–206 (2000).
37. Rebay, I., Fehon, R. G. & Artavanis-Tsakonas, S. Specific truncations of *Drosophila* Notch define dominant activated and dominant negative forms of the receptor. *Cell* **74**, 319–329 (1993).
38. Karpus, O. N. et al. Shear stress-dependent downregulation of the adhesion-G protein-coupled receptor CD97 on circulating leukocytes upon contact with its ligand CD55. *J. Immunol.* **190**, 3740–3748 (2013).
39. Desai, B. S., Chadha, A. & Cook, B. The *stum* gene is essential for mechanical sensing in proprioceptive neurons. *Science* **343**, 1256–1259 (2014).
40. He, L., Binari, R., Huang, J., Falo-Sanjuan, J. & Perrimon, N. In vivo study of gene expression with an enhanced dual-color fluorescent transcriptional timer. *eLife* **8**, e46181 (2019).
41. Krasnoperov, V. et al. Dissociation of the subunits of the calcium-independent receptor of α-latrotoxin as a result of two-step proteolysis. *Biochemistry* **48**, 3230–3238 (2009).
42. Pereanu, W. & Hartenstein, V. Neural lineages of the *Drosophila* brain: a three-dimensional digital atlas of the pattern of lineage location and projection at the late larval stage. *J. Neurosci.* **26**, 5534–5553 (2006).
43. Shearin, H. K., Quinn, C. D., Mackin, R. D., Macdonald, I. S. & Stowers, R. S. t-GRASP, a targeted GRASP for assessing neuronal connectivity. *J. Neurosci. Meth.* **306**, 94–102 (2018).
44. Feinberg, E. H. et al. GFP reconstitution across synaptic partners (GRASP) defines cell contacts and synapses in living nervous systems. *Neuron* **57**, 353–363 (2008).
45. Ito, K., Urban, J. & Technau, G. M. Distribution, classification, and development of *Drosophila* glial cells in the late embryonic and early larval ventral nerve cord. *Rouxs Arch. Dev. Biol.* **204**, 284–307 (1995).
46. Usui, T. et al. Flamingo, a seven-pass transmembrane cadherin, regulates planar cell polarity under the control of Frizzled. *Cell* **98**, 585–595 (1999).
47. Scholz, N., Langenhan, T. & Schöneberg, T. Revisiting the classification of adhesion GPCRs. *Ann. NY Acad. Sci.* **1456**, 80–95 (2019).
48. Blanco-Redondo, B. & Langenhan, T. Parallel genomic engineering of two *Drosophila* genes using orthogonal *attB*/*attP* sites. *G3* **8**, 3109–3118 (2018).
49. Kawasaki, T. & Kawai, T. Toll-Like receptor signaling pathways. *Front. Immunol.* **5**, 461 (2014).
50. Sprinzak, D. et al. *Cis*-interactions between Notch and Delta generate mutually exclusive signalling states. *Nature* **465**, 86–90 (2010).

Methods

Molecular biology

Plasmids generated in this study. For Schneider-2 cell assays: *Act5.1C-p>N$^{\Delta EGF}$-LexA* (pTL221); *Act5.1C-p>N$^{\Delta ECN}$-LexA* (pTL198); *Act5.1C-p>N$^{\Delta ECN/\Delta S3}$-LexA* (pTL354); *Act5.1C-p>CD4-NRS-LexA* (pTL222); *Act5.1C-p>CD4-3TEVs-NRS-LexA* (pTL235); *Act5.1C-p>CD4-6TEVs-NRS-LexA* (pTL228); *Act5.1C-p>SP^{BiP}-CD4-6TEVs-NRS-LexA* (pTL285); *Act5.1C-p>SP^{BiP}-CD4-6TEVs-NRS$^{\Delta S3}$-LexA* (pTL361); *Act5.1C-p>SP^{BiP}-Cirl-NRS-LexA-Flag* (pTL497); *Act5.1C-p>SP^{BiP}-Cirl$^{\Delta GPS(H>A)}$-NRS-LexA-Flag* (pNH93); *Act5.1C-p>SP^{BiP}-Cirl-NRS$^{\Delta S3}$-LexA-Flag* (pNH127); *lexAop>FLuc2* (pTL196); *Act5.1C-p>RLuc* (pTL182); *Act5.1C-p>Tollo* (pAB45); *MT-p>secTEVp* (pTL224); *MT-p>intraTEVp* (pTL351).

For HEK293T cell assays: *CMV-p>SP^{Igκ}-HA-N$^{\Delta EGF}$-LexA* (pAD2); *CMV-p>SP^{Igκ}-HA-Cirl-NRS-LexA-3×Flag* (pAD4); *CMV-p>SP^{Igκ}-HA-Cirl$^{\Delta GPS}$-NRS-LexA-3×Flag* (pAD3); *CMV-p>SP^{Igκ}-HA-Cirl-NRS$^{\Delta S3}$-LexA-3×Flag* (pAD29).

Drosophila transgenes: *Cirl-p>HA-Cirl-NRS-LexA-3×V5-attB* (pTL803); *Cirl-p>HA-Cirl$^{\Delta GPS(H>A)}$-NRS-LexA-3×V5-attB* (pTL804); *Cirl-p>HA-Cirl-NRS$^{\Delta S3}$-LexA-3×V5-attB* (pTL807); *Cirl-p>HA-Cirl-NRS-QF2-attB* (pTL878); *Cirl-p>HA-Cirl-NRS-GAL4-attB* (pTL879); *Cirl-p>RFP-Cirl7TM-2×V5* (pNH189); *Cirl-p>Cirl7TM-2×V5* (pNH191); *Mayo-p>HA-Mayo-NRS-LexA-3×V5-attB* (pTL914); *Mayo-p>HA-Mayo$^{\Delta GPS(H>A)}$-NRS-LexA-3×V5-attB* (pTL915); *Mayo-p>HA-Mayo-NRS$^{\Delta S3}$-LexA-3×V5-attB* (pTL917); *Ketchup-p>HA-Ketchup-NRS-LexA-3×V5-attB* (pTL918); *Ketchup-p>HA-Ketchup$^{\Delta GPS(T>A)}$-NRS-LexA-3×V5-attB* (pTL920); *Ketchup-p>HA-Ketchup-NRS$^{\Delta S3}$-LexA-3×V5-attB* (pTL921); *UAS>nSyb-RFP* (pNH86).

Plasmid construction. All plasmids were constructed using standard molecular biological methods, validated by diagnostic restriction digests (all enzymes from New England BioLabs) and sequencing (Microsynth SeqLab). QuikChange-based PCRs were performed with PfuUltra HF DNA polymerase (Agilent Technologies, 600380-51). All used primers were obtained from Eurofins Genomics and Microsynth SeqLab and are listed in Supplementary Table 1. Primers larger than 60 bp were ordered at gel-filtered high-purity salt-free grade.

Expression clones were generated by Gateway LR recombination (Thermo Fisher Scientific, 11791020) of respective entry vectors with the destination vector pAWF (a gift from T. Murphy; *Drosophila* Gateway Vector Collection; pEntry→pExpression vectors: pTL194→pTL198, pTL213→pTL221, pTL344→pTL354, pTL210→pTL222, pTL227→pTL228, pTL232→pTL235, pTL279→pTL285, pTL359→pTL361, pTL493→pTL497, pNH126→pNH127, pTL178→pTL182), and expression clone pTL196 through LR recombination with destination vector pLOT-W/pTL196 (ref. [51]) according to the manufacturer's protocol.

pTL194 (entry vector for N$^{\Delta ECN}$-LexA): insertion of a 0.7-kbp HindIII/SphI fragment amplified from pTL117 (ref. [52]) (a gift from P. Overton) with primers tl_103F/tl_104R in pTL185. pTL185 is a donor vector generated by amplification of a 1.1-kbp fragment of N$^{\Delta ECN}$ cDNA (a gift from G. Struhl)[35,53] by attB site-flanked primers tl_93F/tl_95R followed by Gateway BP recombination with a pDONR221 vector.

pTL213 (entry vector for N$^{\Delta EGF}$-LexA): ligation of HindIII/AatII fragments of pTL194 (3.5 kbp) and pTL211 (2.7 kbp). pTL211 is a donor vector generated by amplification of a 0.8-kbp SalI/AgeI fragment of N$^{\Delta EGF}$ cDNA (a gift from G. Struhl)[35,53] with primers tl_127F/128R and insertion into pTL204.

pTL344 (entry vector for N$^{\Delta ECN/\Delta S3}$-LexA): amplification of a 0.5-kbp fragment with primers tl_173F/tl_285R (the reverse primer contained the V1763K mutation) of pTL252 and re-insertion into pTL252 with KpnI/RsrII.

pTL210 (entry vector for CD4-NRS-LexA): amplification of a 1.1-kbp AatII/ClaI fragment with primers tl_133F/tl_134R of pTL174 (a gift from R. Kopan) and insertion into pTL194 (N$^{\Delta ECN}$-LexA entry clone).

pTL227 (entry vector for CD4-6TEVs-NRS-LexA): insertion of a double copy of a 0.1-kbp 3×TEVs fragment released through AvrII/SpeI digest from pTL154 into pTL210.

pTL232 (entry vector for CD4-3TEVs-NRS-LexA): digestion of pTL227 with SacII, release of a 3×TEVs fragment, and re-circularization through ligation.

pTL279 (entry vector for SP^{BiP}-CD4-6TEVs-NRS-LexA): insertion of an annealed primer fragment of tl_196F/tl_197R at the AgeI/KpnI sites of pTL275.

pTL359 (entry vector for SP^{BiP}-CD4-6TEVs-NRS$^{\Delta S3}$-LexA): release of a 0.7-kbp fragment containing the V1763K mutation by AvrII/BglII digestion of pTL353 and insertion into pTL279.

pTL493 (entry vector for SP^{BiP}-Cirl-NRS-LexA-Flag): amplification of a 2.7-kbp fragment containing the Cirl cDNA from DGRC clone RE25258 (RRID:DGRC_10101) with primers tl_478F/tl_479R; digestion with AgeI/AvrII and insertion into pTL279.

pNH93: linearization of pTL497 via PstI and insertion of a PCR-amplified 0.9-kbp fragment (primers nh_213/nh_214R) that contains the H672A point mutation via Gibson Assembly (New England BioLabs; E5510S).

pNH126 (entry vector for Act5.1C-p>SP^{BiP}-Cirl-NRS$^{\Delta S3}$-LexA-Flag): QuikChange mutagenesis of pTL493 with primers nh_213/nh_214R to introduce a V–K mutation at the S3 cleavage site.

pTL177 (entry vector for firefly luciferase 2 of *Photinus pyralis*): amplification of a 1.7-kbp DraI/XhoI fragment of pGL4.10 (Promega; E6651) with primers tl_75F/tl_76R and insertion into pENTR1A Dual (Thermo Fisher Scientific, A10462).

pTL178 (entry vector for Renilla Luciferase of *Renilla reniformis*): amplification of a 1.0-kbp DraI/XhoI fragment of pGL4.74 (Promega, E6921) with primers tl_77F/tl_78R and insertion into pENTR1A Dual.

pAB45 was generated by ligation of a 5.3-kbp fragment of pAWF outwardly amplified with primers ab_102F/103R, and a 4.1-kbp fragment containing the Tollo cDNA amplified from DGRC clone LD33590 (RRID: DGRC_2271) with primers ab_104F/105R. Both fragments were digested with DpnI/KpnI/AvrII and ligated; the KpnI site was destroyed during the cloning.

pTL224: amplification of a 0.8-kbp EcoRI/XbaI fragment of pMT-TEV (ref. [54]) (a gift from R. Schuh) using primers tl_141F/tl_142R (the sense primer encoded the BiP secretion signal peptide), which was re-inserted into pMT-TEV.

pTL351: digestion of pTL224 with EcoRI/NheI and insertion of an annealed primer fragment of tl_288F/tl_289R.

pTL803: ligation of a 2.4-kbp BstEII/BstBI fragment of pTL799 (containing a *Cirl-NRS-LexA-3×V5* minigene fragment; custom-synthesized by Thermo Fisher Scientific) with a 11.2-kbp BstEII/BstBI fragment of pTL564 (encoding the *attB*-flanked genomic *Cirl* ORF with an N-terminal HA tag)[10].

pTL804: replacement of a 1.1-kbp BstEII/PacI fragment of pTL803 with a fragment of pTL800; custom-synthesized by Thermo Fisher Scientific).

pTL807: replacement of a 0.2-kbp BstEII/PacI fragment of pTL803 with a fragment of pTL802; custom-synthesized by Thermo Fisher Scientific).

pTL878: ligation of a 12.6-kbp RsrII/NheI fragment of pTL803 with a 1.1-kbp RsrII/SpeI fragment of pTL875 (custom-synthesized by Thermo Fisher Scientific).

pTL879: ligation of a 12.6-kbp FseI/AfeI fragment of pTL878 with a 1.3-kbp fragment of pTL876 (custom-synthesized by Thermo Fisher Scientific). pAD1 was generated by linearization of pDisplay vector via SacII/NotI and insertion of a PCR-amplified 1.2-kbp fragment (primers tl_921F/tl_922R) that contains Notch$^{\Delta ECN}$ (N$^{\Delta ECN}$, pTL198).

pAD2 was generated by linearization of pDisplay vector via SacII/NotI and insertion of a PCR-amplified 3.4-kbp fragment (primers tl_921F/tl_922R) that contains Notch$^{\Delta EGF}$ (N$^{\Delta EGF}$, pTL221).

pAD3 was generated by ligation of a PCR-amplified 3.3-kbp fragment (primers tl_935F/tl_936R) that contains CIRL$^{\Delta GPS}$-NRS-LexA and a 5.2-kbp fragment (primers tl_937F/tl_938R) that contains the pDisplay vector (Thermo Fisher Scientific, V66020).

pAD4 was generated by ligation of a BlpI/MluI-linearized 2.2-kbp fragment that contains CIRL-NRS-LexA (pTL497) and BlpI/MluI-linearized 6.3-kbp pDisplay vector from pAD3.

QuikChange mutagenesis of pAD4 with primers tl_210F/tl_211R yielded pAD29.

pNH189 was custom-synthesized by GeneArt, Invitrogen.

pNH191 was generated by removal of the RFP sequence from pNH189 using AgeI-HF and subsequent self-ligation.

pNH86 was generated through PCR amplification of the nSyb-RFP sequence from template pTL152 using primers nh_187F and nh_188R and ligation into a pTW-attB backbone via NheI and BglII.

Fly experiments

For all experiments involving *Drosophila melanogaster*, animals of the indicated genotype and life stage were randomly selected. Fly genotypes for neuroblast counts were blinded during data analyses; fly genotypes for expression studies could not be blinded due to recognizable specific expression patterns. Data were sampled without sex bias except for leg immobilization experiments, for which only female flies were used.

Fly strains generated in this study. *w^{1118}; $Cirl^{KO}$ {pTL803[HA-Cirl-NRS-LexA-3×V5-attB]}$attP^{Cirl}$ w^- loxP/CyO;;* (LAT498)

w^{1118}; $Cirl^{KO}$ {pTL804[HA-$Cirl^{\Delta GPS(H>A)}$-NRS-LexA-3×V5-attB]}$attP^{Cirl}$ w^- loxP/CyO;; (LAT503)

w^{1118}; $Cirl^{KO}$ {pTL807[HA-Cirl-$NRS^{\Delta S3}$-LexA-3×V5-attB]}$attP^{Cirl}$ w^- loxP/CyO;; (LAT512)

w^{1118}; $Cirl^{KO}$ {pTL803[HA-Cirl-NRS-LexA-3×V5-attB]}$attP^{Cirl}$ w^- loxP, 13×lexAop2-6×mCherry-HA w/CyOGFPw$^-$;;* (LAT755)

w^{1118}; $Cirl^{KO}$ {pTL879[HA-Cirl-NRS-GAL4-3×V5-attB]}$attP^{Cirl}$ w^+loxP/CyO;; (LAT857)

w^{1118}; $Cirl^{KO}$ {pTL879[HA-Cirl-NRS-QF2-3×V5-attB]}$attP^{Cirl}$ w^- loxP/CyO;; (LAT894)

w^{1118};; $Mayo^{KO}$ {pTL914[HA-Mayo-NRS-LexA-3×V5-attB]}$attP^{Mayo}$ DsRed$^-$ loxP/TM3,Sb;; (LAT1220)

w^{1118};; $Mayo^{KO}$ {pTL917[HA-Mayo-$NRS^{\Delta S3}$-LexA-3×V5-attB]}$attP^{Mayo}$ DsRed$^-$ loxP/TM3,Sb;; (LAT1232)

w^{1118};; $Ketchup^{KO}$ {pTL918[HA-Ketchup-NRS-LexA-3×V5-attB]}$attP^{Ketchup}$ DsRed$^-$ loxP/TM3,Sb;; (LAT1238)

w^{1118};; $Ketchup^{KO}$ {pTL920[HA-Ketchup$^{\Delta GPS(T>A)}$-NRS-LexA-3×V5-attB]} $attP^{Ketchup}$ DsRed$^-$ loxP/TM3,Sb;; (LAT1242)

w^{1118};; $Ketchup^{KO}$ {pTL921[HA-Ketchup-$NRS^{\Delta S3}$-LexA-3×V5-attB]}$attP^{Ketchup}$ DsRed$^-$ loxP/TM3,Sb;; (LAT1246)

w^{1118}; $Cirl^{KO}$ {pTL803[HA-Cirl-NRS-LexA-3×V5-attB]}$attP^{Cirl}$ w^- loxP/CyOGFPw$^-$;; (LAT1405)

w^{1118};:Cirl[108/3A.2]{attP$^+$ loxP$^+$}[w$^-$] att{dCirl-NRS-lexA [w$^-$]/ CyOGFPw$^-$;w; P{$w^{+mW.hs}$=GawB}MD806/TM6B,Tb;* (LAT988)

w^{1118}; $Cirl^{KO}$ {w^{+mC}=pNH191[Cirl7TM-2×V5 w^-]}$attP^{Cirl}$/ CyOGFPw$^-$;;(LAT650)

w^{1118}; $Cirl^{KO}$ {w^{+mC}=pNH189[RFP-Cirl7TM-2×V5 w^-]}$attP^{Cirl}$;; (LAT862)

w^{1118}; $Cirl^{KO}$ {w^{+mC}=pNH306[Cirl1TM-V5-T2A-GAL4, Cirl7TM-V5-T2A-LexA w^-]}$attP^{Cirl}$; Kr-GAL4 (LAT1401)

w^{1118}; Syb::RFP w+ attP40/CyO; (TAG172)

w^{1118}; $Cirl^{KO}$ {pTL804[HA-$Cirl^{\Delta GPS(H>A)}$-NRS-LexA-3×V5-attB]}$attP^{Cirl}$ w^- loxP/CyOGFPw$^-$;; (LAT647)

w^{1118}; $Cirl^{KO}$ {pTL807[HA-Cirl-$NRS^{\Delta S3}$-LexA-3×V5-attB]}$attP^{Cirl}$ w^- loxP/ CyOGFPw$^-$;; (LAT649)

w^{1118}; dCirl-GAL4/CyOGFPw$^-$; P{w^{+mC}=UAS-RFP.W}^{3}, P{w^{+m*}=lexAop-2×hrGFP.nls}^{3a} /TM6B, Tb (LAT649)

Published fly strains. BDSC numbers indicated in brackets where applicable.

w^{1118};; Df(3L)BSC578/TM6C, cu^1 Sb^1 (*Tollo* deficiency; 25412)

w;; $Tollo^{C5}$/TM6C, Tb, Sb* (*$Tollo^{KO}$*; a gift from T. Lecuit) (ref. [55])

w; P{$w^{+mW.hs}$=GawB}MD806/TM6B, Tb^1* (*Tollo-GAL4;* 36548) (ref. [56])

y^1 w; $wg^{Sp\text{-}1}$/CyO, P{w^{+mC}=Dfd-EYFP}^{2}; P{$y^{+t7.7}$ w^{+mC}=13×LexAop 2-post-t-GRASP}^{attP2} PBac{$y^{+mDint2}$ w^{+mC}=20×UAS-pre-t-GRASP}^{VK00027}* (79 040; GN345)

w; P{$w^{+mW.hs}$=GawB}MD806/TM6B, Tb^1* (36548; GN282)

w^{1118}; $Cirl^{KO}$ $attP^{Cirl}$ w^- loxP/CyOGFPw$^-$;; (ref. [9])

w^{1118}; $Cirl^{KO}$ {pTL370[$Cirl^{Rescue}$]}$attP^{Cirl}$ w^- loxP/CyOGFPw$^-$;; (=*$Cirl^{WT}$*; ref. [9])

w^{1118}; $Cirl^{KO}$ {pMN44[$Cirl^{H>A}$]}$attP^{Cirl}$ w^- loxP/CyOGFPw$^-$;; (ref. [10])

w^{1118}; $Cirl^{KO}$ {pMN4[$Cirl^{N\text{-}RFP}$]}$attP^{Cirl}$ w^- loxP/CyOGFPw$^-$;; (ref. [10])

w^{1118};; {w^{+m}=pTL471[20×UAS-IVS-Cirl::3×flag]}$attP^2$/TM3, Sb, Kr-GAL4 (ref. [9])

w^{1118}; $dCirl^{KO}$ {w^{+mC}=pTL464[Cirl-p-GAL4]}$attP^{dCirl}$ loxP/CyOGFPw$^-$;; (ref. [9])

y^1 w; $wg^{Sp\text{-}1}$/CyO, P{Wee-P.ph0}$Bacc^{Wee\text{-}P20}$; P{$y^{+t7.7}$ w^{+mC}=20×UAS-6×mCherry-HA}^{attP2}* (52268; GN310)

$y^1$$w^{1118}$;;P{$w^{+mC}$ QUAS-mtdTomato::3×HA} (ref. [26]) (30005; GN129)

w;; UASt-Lifeact::GFP/TM6B, Tb* (a gift from D. Montell)

w^{1118}; P{GMR55B12-GAL4}^{attP2} (cortex glia driver; a gift from C. Klämbt; 39103) (refs. [57,58])

w;; P{$w^{+mW.hs}$ GawB}MD806/TM6B, Tb^1* (*Tollo-p-GAL4*; 36548)

w;; P{w^{+m*}=GAL4}repo/TM3, Sb^1* (*repo-p-GAL4;* 7415)

yw; PBac{$y^{+mDint2}$$w^{+mC}$ 13×lexAop2-6×mCherry::HA}VK00018/CyO; (52272)

yw;; P{$y^{+t7.72}$$w^{+mC}$ 20×UAS-6×GFP}^{attP2} (52262)

yw;20×UAS-6×GFP; lexAop-myr::mCherry (a gift from W. Hütteroth)

w^{1118};;UAS-RFPnls/TM3, Sb^1 (31417)

w^{1118};; P{w^{+mC} lexAop-2×hrGFP.nls}^{3a} (29955)

; ok6-GAL4 w^+; (ref. [59])

w^{1118}; P{w^{+m*}=lexAop-2×hrGFP.nls}^{2a};; (29954)

w^{1118}; +; $Mayo^{KO}$ {pTL789 [Mayo-p-GAL4-attB]}$attP^{Mayo}$ DsRed$^-$ loxP / TM3, Sb;; (ref. [48])

v^1; $Kr^{If\text{-}1}$/CyO; P{$y^{+t7.7}$ $v^{+t1.8}$=UAS-TransTimer.v^+}^{attP2} (a gift from N. Perrimon; 93411)

w^{1118}; phiC31{KK108383}^{w1O0749} (*UAS-Cirl-RNAi*; 100749; GN434)

13×LexAop2-6×mCherry::HA w^+/CyOGFPw$^-$; {20×UAS-6×GFP w^+}^{attP2} (52272 + 52262; LAT649)

Cell culture

Cell lines were authenticated by the vendor by short-tandem-repeat analysis and were continuously tested for mycoplasma contamination.

Schneider-2 cells. Schneider-2 cells were obtained from ThermoFisher Scientific (#R69007) and authenticated by the supplier. Cells were cultured in Schneider's *Drosophila* medium (Thermo Fisher Scientific, 21720-024) supplemented with 10% fetal bovine serum (FBS) (Gibco, Thermo Fisher Scientific, 10500-064). Cultures were maintained in an air incubator at 28 °C. Schneider-2 cells were split and plated into individual wells of a 96-well plate at a concentration of 5×10^5 per well on day 0. Twenty-four hours after plating (day 1), cells were transfected with 0.4 µl Lipofectamine 2000 (Thermo Fisher Scientific, 11668019) per well with the appropriate 1:1 plasmid/reagent mixture according to the manufacturer's instructions and incubated for 48 h. When induction of the metallothionein-promoter was required, $CuSO_4$ stock medium was added 24 h after transfection (day 2) to a final concentration of 0.5 mM. For transfection, mini- or midi-prepped plasmid DNA (Qiagen) for each construct was adjusted to a stock concentration of 100 ng μl^{-1} using a nanophotometer (Implen). For determining the activity of individually expressed NRS proteins, a total amount of 200 ng of DNA per 96-well plate well was transfected and always contained 10 ng of *lexAop>FLuc2* (test construct reporter) and 5 ng of *Act5.1Cp>RLuc* (transfection control reporter). Forty nanograms of test constructs (*X-NRS-LexA*) and TEV protease plasmids were added at 1:1 ratios (equimolarly adjusted to *lexAop>FLuc2*) to the DNA mixes; each DNA mix was supplemented with empty *pBSK-SK*$^+$vector (Stratagene, Agilent, 212205) to the final DNA amount of 200 ng per well. For the assessment of Tollo co-expression on Cirl-NRS-LexA activity, the total transfected

DNA amount was increased to 1,200 ng per well and included increasing amounts of Tollo plasmid DNA (0, 100 and 1,000 ng per well) per condition, whereas the DNA amount of the other co-transfected plasmids was left unchanged (*lexAop>FLuc2*: 10 ng per well; *Act5.1Cp>RLuc*: 5 ng per well; *Cirl-NRS-LexA*: 40 ng per well) and *pBSK-SK*$^+$DNA served as stuffer DNA to reach the final DNA amount per well.

HEK cells. HEK 293 T cells were obained from the German Collection of Microorganisms and Cell Culture (#ACC635) and authenticated by the supplier. Cells were cultured in Dulbecco's modified Eagle's medium (DMEM; Sigma-Aldrich, D6429-500ML) containing 10% FBS (Gibco, 10500-064) and 1% penicillin–streptomycin (Capricorn Scientific, PS-B) in a 37 °C and 5% CO_2 air incubator. On day 0, cells were split with accutase (Invitrogen, Thermo Fisher Scientific, 00-4555-56) and plated out in 96-well plates (Cellstar, Greiner Bio-One, 655180) pretreated for 45 min with 50 µl of 0.01% poly-L-lysine (Sigma-Aldrich, P9404-100MG) per well. Equimolar transfection was performed 24 h later using 25 ng of the NRS-plasmid constructs per well, supplemented by *pBSK-SK*+ stuffer DNA to a total amount of 100 ng DNA per well. The used plasmids were previously mini-prepped (Macherey Nagel, NucleoSpin, 740588.250) and adjusted to a total concentration of 100 ng µl^{-1} using spectrophotometry. Per well, 0.4 µl of Lipofectamine 2000 (Thermo Fisher Scientific, 11668019) was used as a transfection reagent diluted in DMEM without FBS according to the manufacturer's instructions.

Luciferase assays

Schneider-2 cells were lysed on day 3 (48 h after transfection) and luciferase measurements with the Dual-Glo luciferase assay system (Promega, E2920) were performed according to the manufacturer's protocol. In brief, the supernatant was removed from each well by aspiration and cells were incubated with 50 µl of Dual-Glo Reagent per well on a shaker at room temperature for 20 min. Lysates were analysed in 96-well plates with a Victor2 plate reader luminometer (Perkin Elme) or SpectraMax M5 (Molecular Devices). After the first analysis, 50 µl of Dual-Glo Stop & Glo reagent was added and incubated again 20 min at room temperature on a shaker, followed by another luminometer measurement.

Firefly and Renilla luciferase luminescence signals were collected for 10 s. Relative luciferase activity (RLA) was calculated for each sample individually as described previously[60], according to the following formula:

$$\mathrm{RLA}_x = (F_x/R_x)/(\overline{F/R})_{\mathrm{Empty}},$$

where

$$(\overline{F/R})_{\mathrm{Empty}} = \left(\sum_{i=1}^{n} F^i_{\mathrm{Empty}}/R^i_{\mathrm{Empty}}\right)/n,$$

where n = number of control samples; F = Firefly luciferase luminescence signal; R = Renilla luciferase luminescence signal; Empty = lexAop>FLuc2 + Ac5.1p>RLuc + BSK-SK$^+$.

ELISA

Twenty-four hours after transfection, HEK293T cells were fixed in 4% paraformaldehyde (PFA; Fluka, 76240) and blocked for 30 min in 100 µl 1× phosphate-buffered saline (PBS; Gibco, 18912-014) for surface ELISAs or 1× PBS with 0.5% Triton X-100 (5% PBT; Sigma-Aldrich, T9284-100ML) for total ELISAs with 5% normal goat serum (NGS; Goat Serum Donor Herd, Sigma-Aldrich, G6767-500ML), respectively. Cells were incubated for 60 min in 100 µl 1× PBS/0.5% PBT + 5% NGS + 1:1,000 anti-HA-peroxidase high affinity rat monoclonal antibody (clone 3F10, Roche, 12013819001). Cells were washed twice in 180 µl of 1× PBS and a substrate solution consisting of 100 µl of ELISA buffer (0.05 M citric acid (Roth, X863.2), 0.05 M disodium phosphate (Roth, 4984.1), pH = 5), 1 mg µl^{-1} *o*-phenylenediamine (Sigma-Aldrich, P9029-50G) and 1:1,000 H_2O_2. The reaction was stopped with 100 µl of 2.5 M H_2SO_4 (Roth, 9316.2) and absorption measurements at 490-nm wavelength were made with a SpectraMax M5 (Molecular Devices).

Neuroblast count

Neuroblasts were marked with anti-Mir (CD#5-7E9BG5AF4, ab197788, Abcam) immunostaining of L3 larvae. Confocal stacks at the same recording conditions were obtained using a SP8 confocal microscope (Leica). Neuroblasts in each stack were counted using the ImageJ (Fiji) Cell Counter plug-in. Only the most superficial plane of neuroblasts was counted.

t-GRASP

Wandering L3 larvae with the genotype *w^{1118};Cirl-NRS-LexA;Tollo-GAL4/13XLexAop2-post-t-GRASP,20XUAS-pre-t-GRASP* were dissected and fixed as described below. Controls had the genotype *w^{1118};;13XLexAop2-post-t-GRASP,20XUAS-pre-t-GRASP/+*. anti-GFP staining was performed as described previously[43]. ImageJ Fiji (NIH) software was used to process and analyse confocal images. Brain areas were measured using the freehand line tool. Particles in the defined area were counted automatically using a macro written in ImageJ macro language[61]. The spot density (counted spots per brain area) was calculated.

Immunohistochemistry

Wandering L3 larvae were dissected in ice-cold Ca^{2+}-free HL-3 (ref. [62]), fixed using 4% PFA and stained according to established protocols[63]. Antibodies and reagents were used in the following dilutions: rabbit-anti-HA (1:1,000, Cell Signaling Technology, C29F4, RRID:AB_1549585), rabbit-anti-RFP (1:1,000, Antibodies-Online, RRID: AB_10781500), mouse-anti-V5 (1:1,000, Invitrogen, RRID: AB_2556564), rabbit-anti-GFP (1:300, Invitrogen G10362, RRID: AB_2536526), rat-anti-Mir (1:500, Abcam, ab197788), 4',6-diamidino-2-phenylindole (DAPI; 20 mM, 1:5,000, Thermo Fisher Scientific, 62249), anti-horseradish peroxidase conjugated with Alexa Fluor-488 (1:250, Jackson ImmunoResearch, 123-545-021, RRID: 2338965) or Cy3 (1:250, Jackson ImmunoResearch, 123-165-021, RRID: AB_2338959), Cy5-conjugated goat-anti-rabbit (1:250, Jackson ImmunoResearch, 111-175-144, RRID: AB_2338013), Cy3-conjugated goat-anti-rat (1:250, Invitrogen, A10522, RRID: AB_2534031), Cy3-conjugated goat-anti-rabbit (111-165-003, RRID: AB_2338000) and goat-anti-mouse antibodies (115-165-146, RRID: AB_2338690, both 1:250, Jackson ImmunoResearch).

Immunoblots

For western blot analyses of Cirl, fly heads were collected into 0.5-ml Eppendorf tubes and immediately frozen in liquid nitrogen. Next, heads were mechanically crushed in 40 µl of 2% SDS supplemented with protease inhibitor cocktail (Sigma-Aldrich, P9599, 1:1,000) using a glass pestle. Samples were incubated on ice for 10 min before the addition of 4 µl Triton X-100 (10%). Next, SDS-based sample buffer (LI-COR) was supplemented with β-mercaptoethanol and was added to a final dilution of 1×. Samples were centrifuged for 30 min at 14,000 rpm (4 °C) and supernatant was collected. The centrifugation step was repeated and supernatant was collected in a fresh tube.

Sample preparation of Ketchup-NRS and Mayo-NRS proteins for western blots and of Cirl protein for mass-spectrometric analyses: one-to two-day-old pupae (around 600 mg per genotype; experiment: RFP-Cirl^{7TM}-2×V5; fluorescence control: nSyb-RFP) were collected and immediately frozen in liquid nitrogen before homogenization in a pre-cooled mortar using a pestle. The resulting protein powder was transferred into a pre-cooled tube and supplemented with homogenization buffer (50 mM Tris-HCl, 150 mM NaCl, 1% Triton X-100, protease inhibitor; 1:1,000, 1 mM DTT, 0.5 mM PMSF). Samples were further homogenized using an Ultra-Turrax (4 × 15 s; IKA T10 Basic) and a glass homogenizer (20× mechanically crushed per sample). Next, samples

were centrifuged at 4,000 rpm for 30 min, again at 13,000 rpm for 30 min and finally at 25,000 rpm for 30 min. The supernatant was collected after each centrifugation step; an aliquot of the supernatant served as input control. To immunoprecipitate Cirl, 75 µl immunomagnetic beads (Chromotek, rtma-100) were washed three times with 500 µl dilution buffer (10 mM Tris-HCl, 150 mM NaCl, 0.5 mM EDTA, pH 7.5) before supernatant incubation. After 3.5 h of incubation, the beads were separated from the supernatant and washed three times with 1× TBS. Proteins were eluted by a 30-min incubation step at 27 °C (800 rpm) in 60 µl elution buffer (2 mM urea, 50 mM Tris-HCl pH 7.5 and 5 µg ml^{-1} trypsin). Supernatant was collected. To collect residual protein from the beads they were washed twice with 25 µl washing buffer (containing 2 M urea, 50 mM Tris-HCl, 1 mM DTT), which was added to the previously collected supernatant and left at room temperature overnight. To immunoprecipitate Ketchup and Mayo, 75 µl of immunomagnetic V5 beads (Chromotek) were used. Supernatant incubation was done at 4 °C for 2 h with end-over-end rotation; 50 µl of 2× SDS sample buffer (LI-COR) supplemented with β-mercaptoethanol was added to the beads and incubated at 95 °C for 10 min. The beads were separated and the supernatant was kept for western blotting. The samples were subjected to electrophoresis on 4–12 % Tris-Glycin SDS gel (Novex-Wedge-Well; Invitrogen) and blotted onto a nitrocellulose membrane (0.2 µm pore size). The membrane was blocked for 1 h at room temperature using Odyssey Blocking buffer (LI-COR) diluted 1:2 with 1× PBS. Blots were probed with primary antisera at the indicated concentrations overnight at 4 °C or 1 h at room temperature: rabbit-anti-HA (1:1,000, RRID: AB_10693385), mouse-anti-V5 (1:500, RRID: AB_2556564), mouse-anti-tubulin-β (1:5,000, RRID: AB_528499), mouse-anti-tubulin-β (1:5,000, DSHB e7, RRID: AB_528499), mouse-anti-spectrin-α (1:1,000, DSHB 3A9, RRID: AB_528473). After rinsing twice and three 10-min washing steps, membranes were incubated with IRDye 680RD goat-anti-rabbit (RRID: AB_2721181) or goat-anti-mouse (RRID: AB_2651128) as well as 800CW goat-anti-mouse (1:15,000; RRID: AB_2687825) or goat-anti-rabbit (1:15,000; RRID:AB_2651127) for 1 h at room temperature, and again rinsed twice and washed three times for 10 min. Blots were imaged with an OdysseyFc 2800 (LI-COR).

Mass spectrometry and data analysis

Mass spectrometry (MS) analysis was performed on an Ultimate3000 RSLC system coupled to an Orbitrap Fusion Tribrid mass spectrometer (Thermo Fisher Scientific). Tryptic peptides were loaded onto a µPAC Trapping Column with pillar diameter of 5 µm, inter-pillar distance of 2.5 µm, pillar length/bed depth of 18 µm, external porosity of 9%, bed channel width of 2 mm and length of 10 mm; pillars are superficially porous with a porous shell thickness of 300 nm and pore sizes in the order of 100 to 200 Å at a flow rate of 10 µl per min in 0.1% trifluoroacetic acid in HPLC-grade water. Peptides were eluted and separated on the PharmaFluidics µPAC nano-LC column: 50 cm µPAC C18 with a pillar diameter of 5 µm, inter-pillar distance of 2.5 µm, pillar length/bed depth of 18 µm, external porosity of 59%, bed channel width of 315 µm and bed length of 50 cm; pillars are superficially porous with a porous shell thickness of 300 nm and pore sizes in the order of 100 to 200 Å by a linear gradient from 2% to 30 % of buffer B (80% acetonitrile and 0.08% formic acid in HPLC-grade water) in buffer A (2% acetonitrile and 0.1% formic acid in HPLC-grade water) at a flow rate of 300 nl per min. The remaining peptides were eluted by a short gradient from 30% to 95% buffer B; the total gradient run was 120 min. MS parameters were as follows: for full MS spectra, the scan range was 335–1,500 with a resolution of 120,000 at $m/z = 200$. MS/MS acquisition was performed in top speed mode with a 3-s cycle time. The maximum injection time was 50 ms. The AGC target was set to 400,000 and the isolation window was 1.6 m/z. Positive ons with charge states 2–7 were sequentially fragmented by higher-energy collisional dissociation. The dynamic exclusion duration was set to 60 s and the lock mass option was activated and set to a background signal with a mass of 445.12002.

MS data analysis was performed using the MaxQuant software v.1.6.17.0 (ref. [64]). Trypsin was selected as the digesting enzyme with a maximum of two missed cleavages. Cysteine carbamidomethylation was set for fixed modifications; oxidation of methionine and deamidation of asparagine and glutamine were specified as variable modifications. The data were analysed using the LFQ method. The first search peptide tolerance was set to 20, and the main search peptide tolerance to 5 ppm. For peptide and protein identification, the *Drosophila melanogaster* subset of the SwissProt database (release 2020_10) was used, and contaminants were detected using the MaxQuant contaminant search. A minimum peptide number of 1 and a minimum length of 6 amino acids was tolerated. Unique and razor peptides were used for LFQ quantification. The match between run option was enabled with a match time window of 0.7 min and an alignment time window of 20 min. For the MaxQuant identification search, protein and peptide spectral match FDR were set to a minimum of 0.01, and proteins were only accepted to be quantified if they were identified in at least two replicates out of three biological replicates for each bait group. Statistical analysis including LFQ ratio, and one-sided significance A test calculation to identify putative interactors of bait proteins was done using the Perseus software suite v.1.6.15.0 (ref. [65]). Putative interactors of Cirl and their subcellular localization were analysed using database entries from Uniprot. MS datasets were submitted to the ProteomeXchange platform (submission reference: 1-20220512-140556).

Imaging

All confocal imaging data were obtained on a Leica TCS SP8 confocal set-up, except the Schneider-2 cell images, which were obtained with a Zeiss LSM 5 system and processed with ImageJ2, Fiji v.2-3-0 or v.1.53q, Zeiss ZEN, and Leica LAS X software suites. Microphotographs of intact adult flies were obtained through a digital camera fitted to a Leica MZ10 F fluorescence stereo microscope.

For low-resolution micrographs of binary expression profiles of Cirl-NRS-LexA, Cirl-NRS-GAL4 and Cirl-NRS-QF2 activities in the legs and heads, adult flies expressing the respective NRS transgene and a suitable transgenic reporter were selected three to five days after eclosion. The legs and head were severed from the abdomen of the anaesthetized flies and placed directly into Vectashield (H-1000, Vector Laboratories). The organs were then mounted onto a cover slip and imaged on a Leica TCS SP8 confocal set-up, and the images were analysed using ImageJ Fiji.

Leg immobilization experiment and TransTimer imaging

Female flies three to five days after eclosion were used in this experiment. A custom-made adhesive for fly fixation was produced as previously described[66]. To extract the glue layer from Scotch tape (Tesa 4124), a 20-cm piece was incubated in 10 ml *n*-heptane (Merck). The tape and *n*-heptane were incubated on a HulaMixer (Thermo Fisher Scientific) overnight at room temperature. Open heptane was handled in a fume hood. After the tape was discarded, the glue–heptane solution could be stored for several weeks at room temperature. The solution was brushed (a spot of around 1 cm) on a 1% agarose/apple-juice plate and allowed to dry for 10–20 s. Subsequently, a CO_2-anaesthetized fly was glued to the surface by its dorsum and wings.

Imaging of *Cirl-NRS-GAL4>UAS-TransTimer* flies was performed on a Leica DM6B upright microscope equipped with a 10×, 0.32 NA dry objective and an sCMOS camera (Leica DFC9000GTC). A blond human hair (around 3 cm long) was dipped into the glue solution, and then the glue-containing end of the hair was put in contact with the distal end of the right metathoracic leg for approximately 10 s until they firmly adhered to each other. The leg was then gently stretched to full extension by pulling at the hair restraint using forceps, and the opposite end of the hair was glued onto the agar plate. Subsequently, the first set of dGFP and RFP signals in the mechanosensory neurons of the femorotibial joints were taken in the immobilized and the mobile

contralateral legs under transient CO_2 anaesthesia (t = 0 h; capturing signals of the pre-immobilization interval). After allowing the legs of the fly to move for 5 h at room temperature without anaesthesia, the fly was re-anaesthetized and the same leg-joint neurons were imaged again (t = 5 h; capturing signals of the immobilization interval). Finally, the hair was cut with scissors, allowing free movement of the previously immobilized leg for another 5 h followed by another imaging session under anaesthesia (t = 10 h; capturing signals of the remobilization interval). For analysis in ImageJ Fiji (NIH) the experimenter was blinded to the experimental conditions. To quantify the dGFP and RFP signals, the mean intensity in a circular region of interest (diameter 5.2 µm) within the mechanosensory neuron was measured for each channel separately. dGFP/RFP ratios were calculated and plotted using Prism. The data distribution of joint angles and dGFP/RFP ratios of *Cirl-NRS-GAL4>UAS-TransTimer* in the leg-joint immobilization experiments were initially tested with a Shapiro–Wilk test. Statistical comparison of sets of repeated dGFP/RFP ratio measurements (at t = 0, 5 and 10 h), each obtained from the same femorotibial joint of the right metathoracic leg, was conducted using a repeated-measures one-way ANOVA with Geisser–Greenhouse correction, followed by a Tukey's multiple comparisons test (for normally distributed samples) or a Friedman test followed by a Dunn's multiple comparisons test (for non-normally distributed samples).

Quantification of leg movements

Quantification of immobilized and mobile leg-bending angles were conducted under similar immobilization and recording conditions. Flies were given 2 min to recover from CO_2 anaesthesia at each protocol phase and were then videotaped for 8 min under each experimental condition using an MZ10 F microscope (Leica) connected to a 190 MC HD camera (Leica) at a frame rate of 30 Hz in MP4 format. The frame rate was reduced to 1 Hz in Adobe Photoshop, exported as a TIFF movie and loaded into ImageJ Fiji (NIH). Seven to ten movement bursts occurred on average in a 8-min video recording. The angular amplitude of the femorotibial joint was measured using the 'Angle tool'. Angle data were averaged for each leg at each of the three experimental intervals (pre-immobilization, immobilization and remobilization) using Prism.

Statistics

All datasets, except MS datasets, were analysed with Prism v.7-9 (GraphPad). Sample sizes were not predetermined by statistical methods. Data distribution was initially tested with a Shapiro–Wilk test. Two-set comparisons were performed with a two-tailed unpaired t-test (for normally distributed samples) or a Mann–Whitney U test (for non-normally distributed samples). If not indicated otherwise, multiple comparison analyses of more than two datasets were conducted with an ordinary one-way ANOVA followed by Tukey's multiple comparison test (for normally distributed samples), or a Kruskal–Wallis test followed by Dunn's multiple comparisons test (for non-normally distributed samples).

Reporting summary

Further information on research design is available in the Nature Portfolio Reporting Summary linked to this article.

Data availability

All datasets plotted in diagrams are available in Source Data. Interactome datasets on Cirl ligands are available at ProteomeXchange with the unique identifier PXD033873. The raw western blot data are available at Figshare at https://doi.org/10.6084/m9.figshare.21930960. All other data are available upon request to the corresponding authors. Source data are provided with this paper.

51. Diegelmann, S., Bate, M. & Landgraf, M. Gateway cloning vectors for the LexA-based binary expression system in *Drosophila*. *Fly* **2**, 236–239 (2008).
52. Lai, S.-L. & Lee, T. Genetic mosaic with dual binary transcriptional systems in Drosophila. *Nat. Neurosci.* **9**, 703–709 (2006).
53. Struhl, G. & Adachi, A. Requirements for presenilin-dependent cleavage of notch and other transmembrane proteins. *Mol. Cell* **6**, 625–636 (2000).
54. Harder, B. et al. TEV protease-mediated cleavage in *Drosophila* as a tool to analyze protein functions in living organisms. *Biotechniques* **44**, 765–772 (2008).
55. Baas, S. et al. Sugar-free frosting, a homolog of SAD kinase, drives neural-specific glycan expression in the *Drosophila* embryo. *Development* **138**, 553–563 (2011).
56. Ayyar, S. et al. NF-κB/Rel-mediated regulation of the neural fate in *Drosophila*. *PLoS ONE* **2**, e1178 (2007).
57. Pogodalla, N. et al. Drosophila ßHeavy-Spectrin is required in polarized ensheathing glia that form a diffusion-barrier around the neuropil. *Nat. Commun.* **12**, 6357 (2021).
58. Li, H.-H. et al. A GAL4 driver resource for developmental and behavioral studies on the larval CNS of *Drosophila*. *Cell Rep.* **8**, 897–908 (2014).
59. Sanyal, S. Genomic mapping and expression patterns of *C380*, *OK6* and *D42* enhancer trap lines in the larval nervous system of *Drosophila*. *Gene Expr. Patterns* **9**, 371–380 (2009).
60. Potter, C. J., Tasic, B., Russler, E. V., Liang, L. & Luo, L. The Q system: a repressible binary system for transgene expression, lineage tracing, and mosaic analysis. *Cell* **141**, 536–548 (2010).
61. Ljaschenko, D., Ehmann, N. & Kittel, R. J. Hebbian plasticity guides maturation of glutamate receptor fields in vivo. *Cell Rep.* **3**, 1407–1413 (2013).
62. Stewart, B. A., Atwood, H. L., Renger, J. J., Wang, J. & Wu, C.-F. Improved stability of *Drosophila* larval neuromuscular preparations in haemolymph-like physiological solutions. *J. Comp. Physiol.* **175**, 179–191 (1994).
63. Schmid, A. & Sigrist, S. J. in *Drosophila, Methods and Protocols* 1st edn (ed. Dahmann, C.) 239–251 (2008).
64. Tyanova, S., Temu, T. & Cox, J. The MaxQuant computational platform for mass spectrometry-based shotgun proteomics. *Nat. Protoc.* **11**, 2301–2319 (2016).
65. Tyanova, S. et al. The Perseus computational platform for comprehensive analysis of (prote)omics data. *Nat. Methods* **13**, 731–740 (2016).
66. Schmied, C. & Tomancak, P. in *Drosophila, Methods and Protocols* 2nd edn (ed. Dahmann, C.) 189–202 (2016).
67. Tuthill, J. C. & Wilson, R. I. Parallel transformation of tactile signals in central circuits of *Drosophila*. *Cell* **164**, 1046–1059 (2016).

Acknowledgements This work was supported by grants from the Deutsche Forschungsgemeinschaft to N.S. and T.L. through FOR2149, project numbers 265903901 (project P01) and 265996823 (project P03) and through CRC 1423, project number 421152132 (projects A06 and B06); and by a junior research grant from the Faculty of Medicine, Leipzig University, to N.S. We thank C. Klämbt, R. Kopan, D. Montell, N. Perrimon, M. Rossner, R. Schuh, G. Struhl and W. Hütteroth for sharing materials and protocols; M. Ueffing for help with MS analyses; T. Lecuit for discussions on the Cirl–Tollo interaction; and L. Abicht, P. Beckmann, A. Böhme, H. Holzinger, K. Heise, S. Lautenschläger, M. Oppmann, S. Schmidt, U. Strobel and P. Tarlatt for technical assistance. Stocks obtained from the Bloomington Drosophila Stock Center (NIH P40OD018537) and Vienna Drosophila Resource Center (VDRC) were used in this study.

Author contributions N.S. and T.L. conceived the study, designed, performed and analysed the experiments, prepared figures and wrote the manuscript with consent from all co-authors. N.S.: cloning, luciferase assays, transgene generation, immunohistochemistry, fly genetics, imaging, protein extraction and MS and western blot analyses. A.-K.D.: cloning, fly genetics, immunohistochemistry, imaging and t-GRASP analyses. M.K. and A.M.-M.: ELISA and luciferase experiments. A.B.: protein extraction, MS and western blot analyses and luciferase experiments. G.M.A.: cell marker expression analyses. M.B.K.: immunohistochemical stainings. F.V.C.: Mayo-NRS and Ketchup-NRS expression profiles. L.F.E.: fly genetics and imaging. H.S.: fly genetics. M. Buhlan and D.L.: joint bending and TransTimer analyses. Y.K.C.: cloning and ELISA experiments. B.B.-R.: Mayo-NRS and Ketchup-NRS protein analyses. F.K. and M.A.J.: MS analyses. M. Bigl: protein extraction, MS and western blot analyses and ELISA experiments. T.L.: cloning, luciferase assays, transgene generation, fly genetics, imaging and quantification of cell marker expression.

Competing interests N.S. and T.L. are co-inventors of a pending patent covering NTF release sensors for aGPCRs (WO/2022/063915; priority application: EP 3974535; applicant: Leipzig University) covered in this manuscript. The remaining authors declare no competing interests.

Additional information

Supplementary information The online version contains supplementary material available at https://doi.org/10.1038/s41586-023-05802-5.

Correspondence and requests for materials should be addressed to Nicole Scholz or Tobias Langenhan.

Peer review information *Nature* thanks Gregory Tall and the other, anonymous, reviewer(s) for their contribution to the peer review of this work. Peer reviewer reports are available.

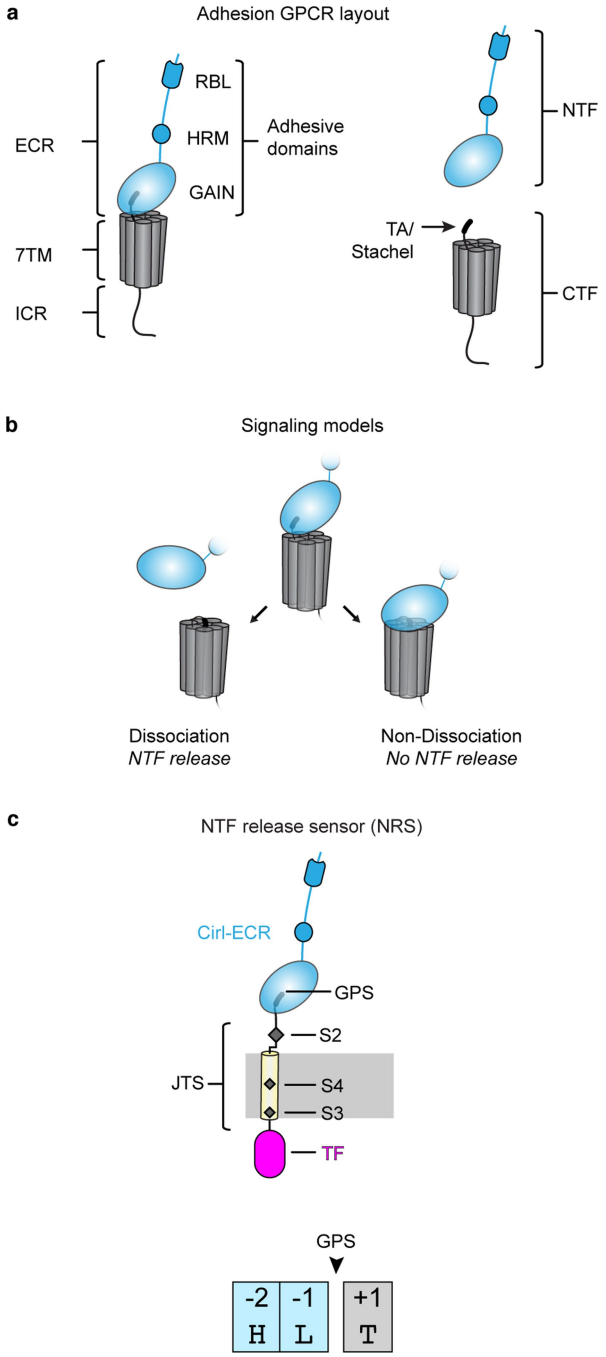

Extended Data Fig. 1 | Structure–function relationships of aGPCRs and functionality of the NRS technique. a, aGPCRs are composed of extra- (ECR) and intracellular regions (ICR) as well as a heptahelical transmembrane-spanning domain (7TM). Owing to autocatalytic cleavage by the GPCR autoproteolysis-inducing (GAIN) domain, most aGPCRs exist as non-covalently stabilized heterodimers composed of an N- (NTF) and C-terminal fragment (CTF), which are affixed to each other by the GAIN domain that contains the tethered agonist (TA)/Stachel. The latrophilin-like Cirl receptor contains rhamnose-binding lectin (RBL) and hormone-receptor motif (HRM) domains in its ECR. **b**, Two principle aGPCR activation modes have received evidence and either do (*Dissociation model*) or do not (*Non-Dissociation model*) rely on aGPCR heterodimer separation. **c**, The NRS consists of the ECR of a given adhesion GPCR including the autoproteolytically active GAIN domain with its GPCR proteolysis site (GPS) fused to the juxta- and transmembrane segment (JTS) of the *Drosophila* Notch receptor and an intracellular heterologous transcription-factor (TF) unit. The JTS contains the recognition sites for cleavage by metallo- and intramembrane proteases (S2–S4). The protein sequence at the GPS used in the Cirl-NRS is shown.

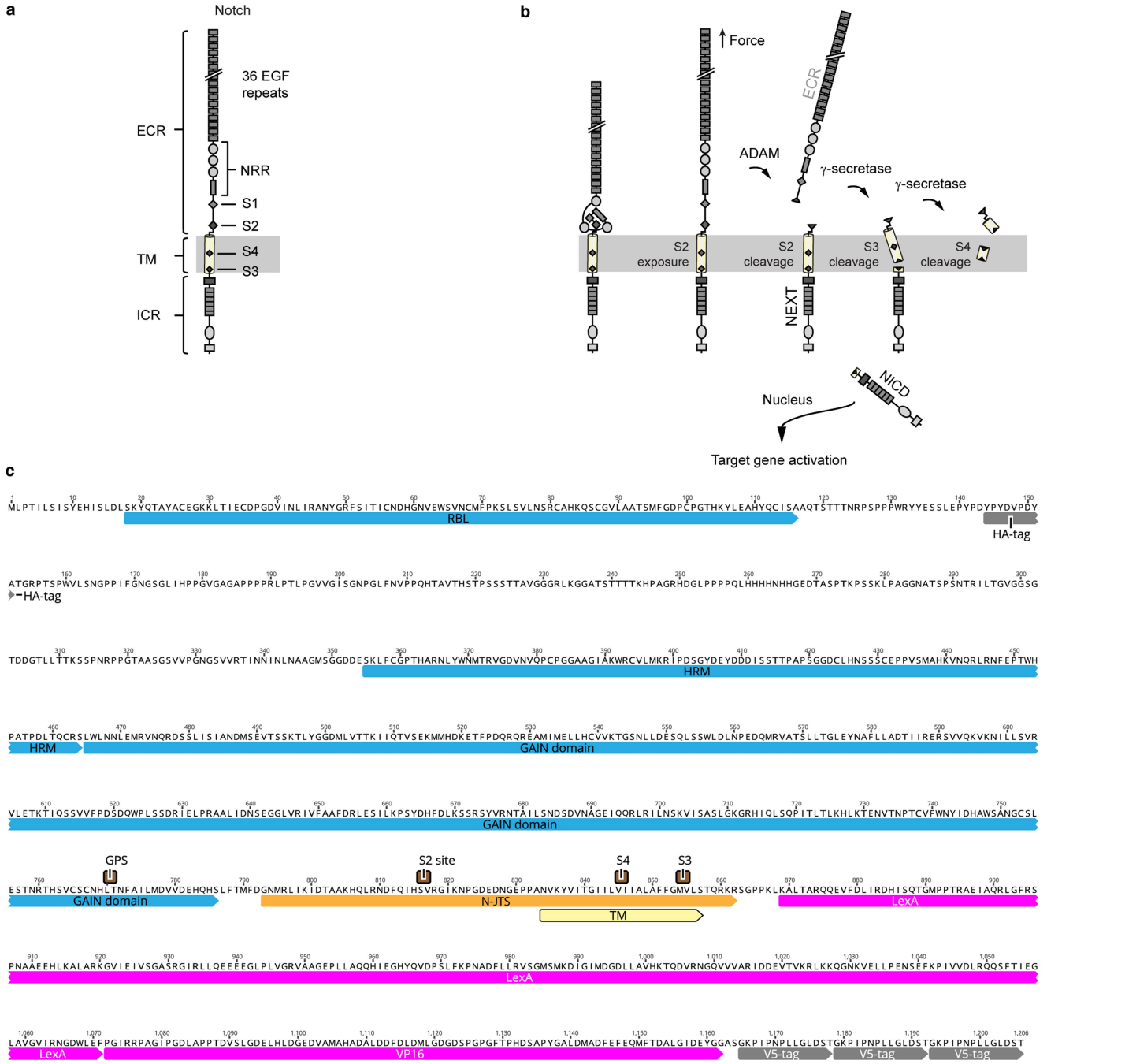

Extended Data Fig. 2 | Activation of the Notch receptor pathway. **a**, Structural layout of the *Drosophila* Notch receptor protein with its ECR containing numerous epidermal growth factor (EGF) domains, the negative regulatory region (NRR), which physiologically suppresses the staggered proteolytic processing at various cleavage sites (S2–S4) until receptor stimulation, and the ICR with sequences involved in nuclear import of the Notch intracellular domain (NICD) and co-activation of gene transcription. **b**, Sequence of events that correspond to Notch processing and transmembrane signal transduction and involved proteases[31]. **c**, Amino acid sequence and domain and motif annotation of the Cirl-NRS-LexA protein. ADAM, A disintegrin and metalloproteinase; ECR, extracellular region; ICR, intracellular region; TM, transmembrane domain.

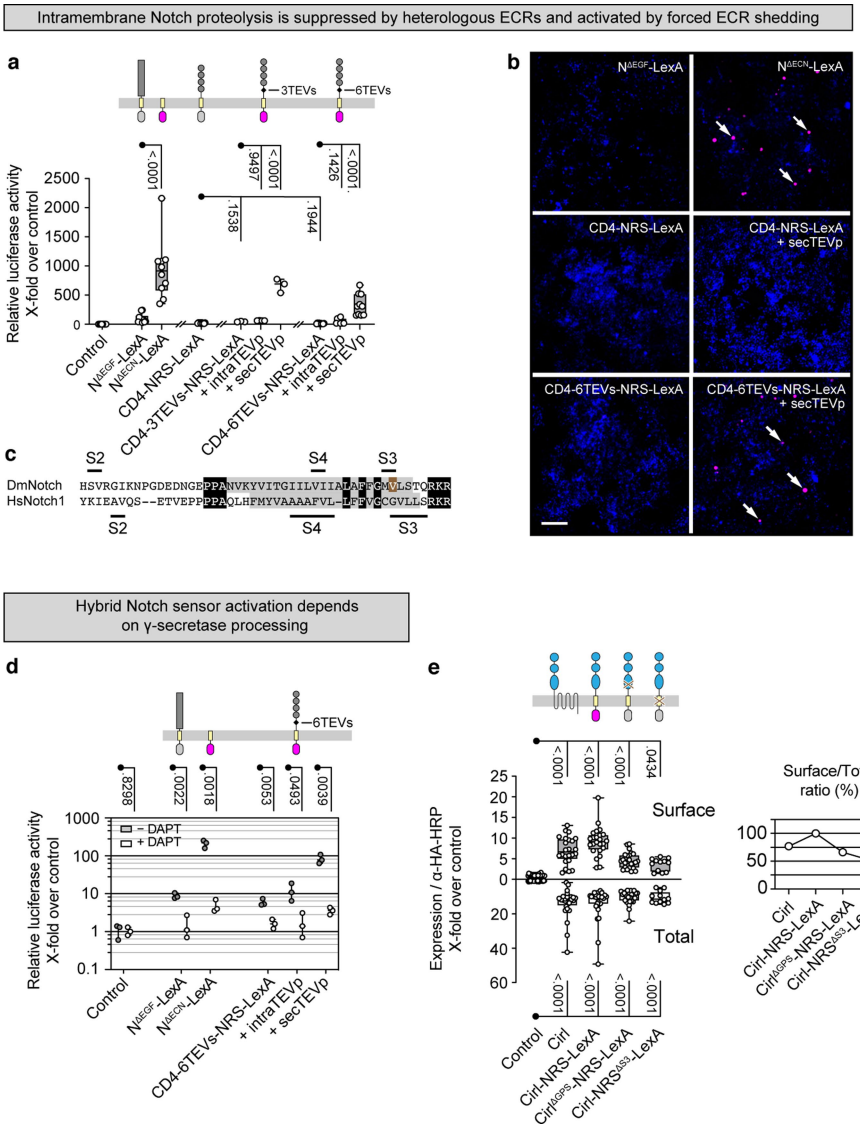

Extended Data Fig. 3 | In vitro characterization of NRS activation. **a**, Characterization of hybrid transmembrane sensors containing the ECR of the human CD4 receptor fused to the Notch^{JTS}-LexA module (CD4-NRS-LexA) in *Drosophila* Schneider-2 cells using a luciferase-based assay. Addition of the CD4-ECR to the NRS basis (CD4-NRS-LexA) suppresses NRS activity. When the CD4-ECR is severed by secTEVp at cognate TEVp at TEVs interposed between CD4 and NRS-LexA components of the sensor (CD4-3TEVs-NRS-LexA, CD4-6TEVs-NRS-LexA), it becomes activated (magenta). Co-expression of cleavable sensors and intraTEVp does not result in sensor activation (grey). N$^{\Delta EGF}$-LexA/N$^{\Delta ECN}$-LexA set, CD4-3TEVs-NRS-LexA set and CD4-6TEVs-NRS-LexA set were tested in separate assays but are displayed in the same graph. Data (n = 10 biological replicates from three independent experiments for all groups, except CD4-3TEVs-NRS-LexA group n = 3 from one experiment) were normalized and presented as multiples of control dataset in box-whisker plots (all data points plotted; horizontal line represents median, boxes the 25th and 75th percentiles, whiskers minimum and maximum values). N$^{\Delta EGF}$-LexA/N$^{\Delta ECN}$-LexA groups were compared with two-tailed Mann–Whitney U test, CD4-3TEVs-NRS-LexA dataset by ordinary one-way ANOVA with Tukey's test, CD4-6TEVs-NRS-LexA dataset with Kruskal–Wallis one-way ANOVA with Dunn's test (confidence interval = 95 % for all comparisons). *P* values are displayed above data. See also Source Data. **b**, NRS-LexA activity of the same sensor set as in **a**, visualized through expression of a *lexAop-DsRed* reporter (CD4-3TEVs-NRS-LexA not shown). Representative confocal images of Schneider-2 cell cultures with NRS-LexA signals (magenta, arrows) counterstained with Hoechst (blue). Scale bar = 100 µm. Experiment was independently repeated 3x with similar results. **c**, Protein sequence alignment of the JTS of *Drosophila* (Uniprot: P07207) and human Notch1 receptors (Uniprot: P46531). Positions of the TM helix (grey box) and S2, S3 and S4 protease cleavage sites are indicated. For control sensors in this study the critical valine residue at the S3 cleavage site (light brown box) was point mutated (V1763K). Black boxes delineate highly conserved residues. **d**, Function of N$^{\Delta ECN}$-LexA and CD4-6TEVs-NRS-LexA variants (grey circles) requires γ-secretase activity as application of 10 µM DAPT suppresses their activation (white circles). Data (n = 3 biological replicates from one experiment for all groups) are presented as multiples of control dataset in box-whisker plots (all data points plotted; horizontal line represents median, whiskers minimum and maximum values). Data groups (-DAPT/+DAPT for each sensor) were compared with two-tailed unpaired *t*-test (confidence interval = 95 %). *P* values are displayed above data. See also Source Data. **e**, Surface and total expression quantified by ELISA shows that Cirl-NRS-LexA variants as shown in **b** are delivered to the cell surface. Surface (n = 24 biological replicates from six independent experiments for all groups, except Cirl-NRS$^{\Delta S3}$-LexA group n = 12 biological replicates from three independent experiments) and total ELISA data (n = 28 biological replicates from seven independent experiments for all groups, except Cirl-NRS$^{\Delta S3}$-LexA group n = 12 biological replicates from three independent experiments) were normalized and presented as multiples of control dataset in box-whisker plots (all data points plotted; horizontal line represents median, boxes the 25th and 75th percentiles, whiskers minimum and maximum values). Data were analysed with Kruskal–Wallis one-way ANOVA with Dunn's test (confidence interval = 95 % for all comparisons). *P* values are displayed above and below data. Surface/total expression ratio (right panel) normalized to Cirl-NRS-LexA ratio indicates degree of surface trafficking of each Cirl-NRS-LexA variant and Cirl. See also Source Data.

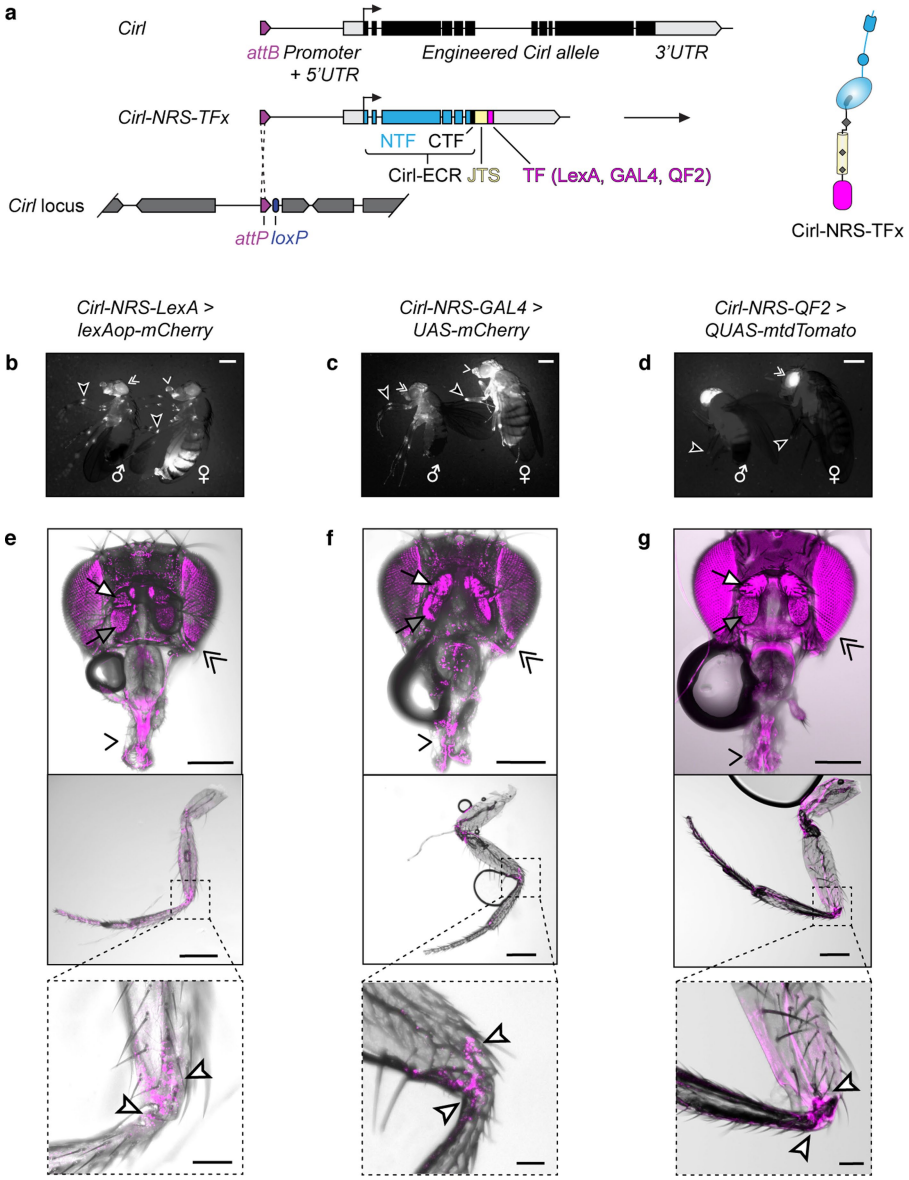

Extended Data Fig. 4 | Comparison of Cirl-NRS activity with different binary expression system readouts. a, Organization of the *Cirl* locus, *Cirl-NRS* alleles and their gene products. **b**–**d**, Cirl-NRS-LexA (**b**), Cirl-NRS-GAL4 (**c**) and Cirl-NRS-QF2 (**d**) sensors display comparable activity in adults in neurons of the proboscis (chevron), eyes (double chevron) and leg joints (arrowheads). Reporter transgene are: *13xLexAop2-6xmCherry-HA* (**b**), *20xUAS-6xmCherry-3xHA* (**c**) and *QUAS-mtdTomato-3xHA* (**d**). Scale bars = 0.5 mm. **e**–**g**, Cirl-NRS dissociation signals reported using the (**e**) LexA/lexAop, (**f**) GAL4/UAS and (**g**) QF2/QUAS binary expression systems. Top panels show Cirl-NRS activity in the eyes (double chevrons), proboscis (chevrons), and the pedicel (white arrows) and funiculus (grey arrows) of the antenna. Middle panels show Cirl-NRS activity in the leg, bottom panels show a close-up of the femorotibial joint with Cirl-NRS-positive mechanosensory neurons (white arrowheads). Scale bars = 250 µm (heads and legs), 50 µm (joints). All experiments independently repeated 3x with similar results.

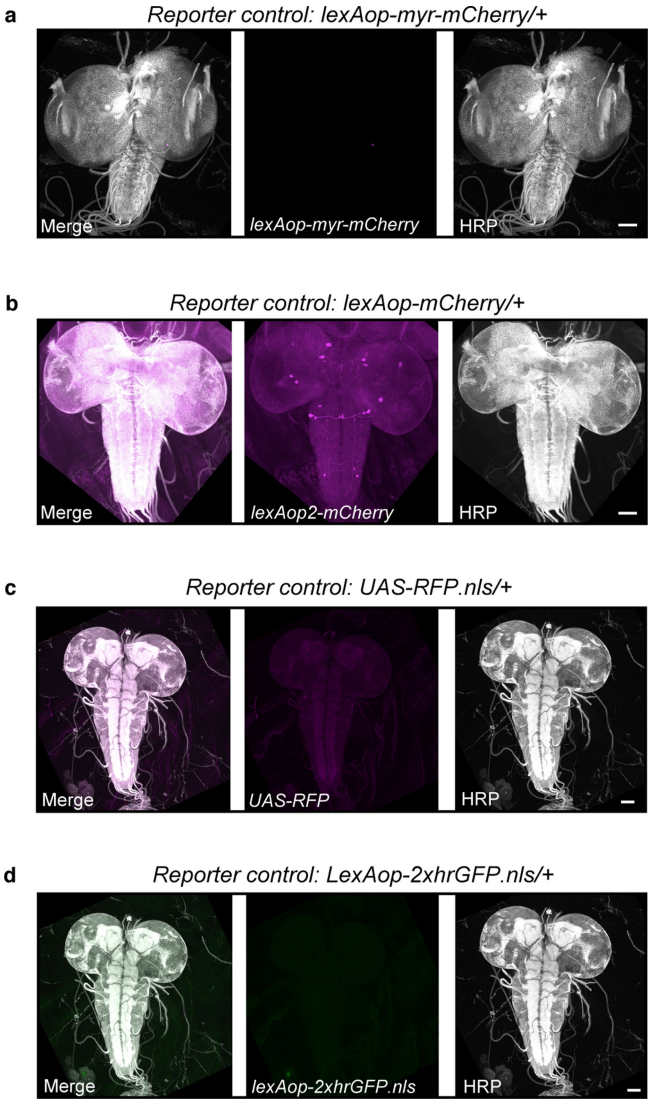

Extended Data Fig. 5 | Binary expression system controls. a, Expression control of *lexAop-myr-mCherry*. **b**, Expression control of *lexAop2-mCherry*. **c**, Expression control of *UAS-RFP.nls*. **d**, Expression control of *2xhrGFP.nls*. Scale bars = 50 µm. Same fly as in **c** expressing both reporters.

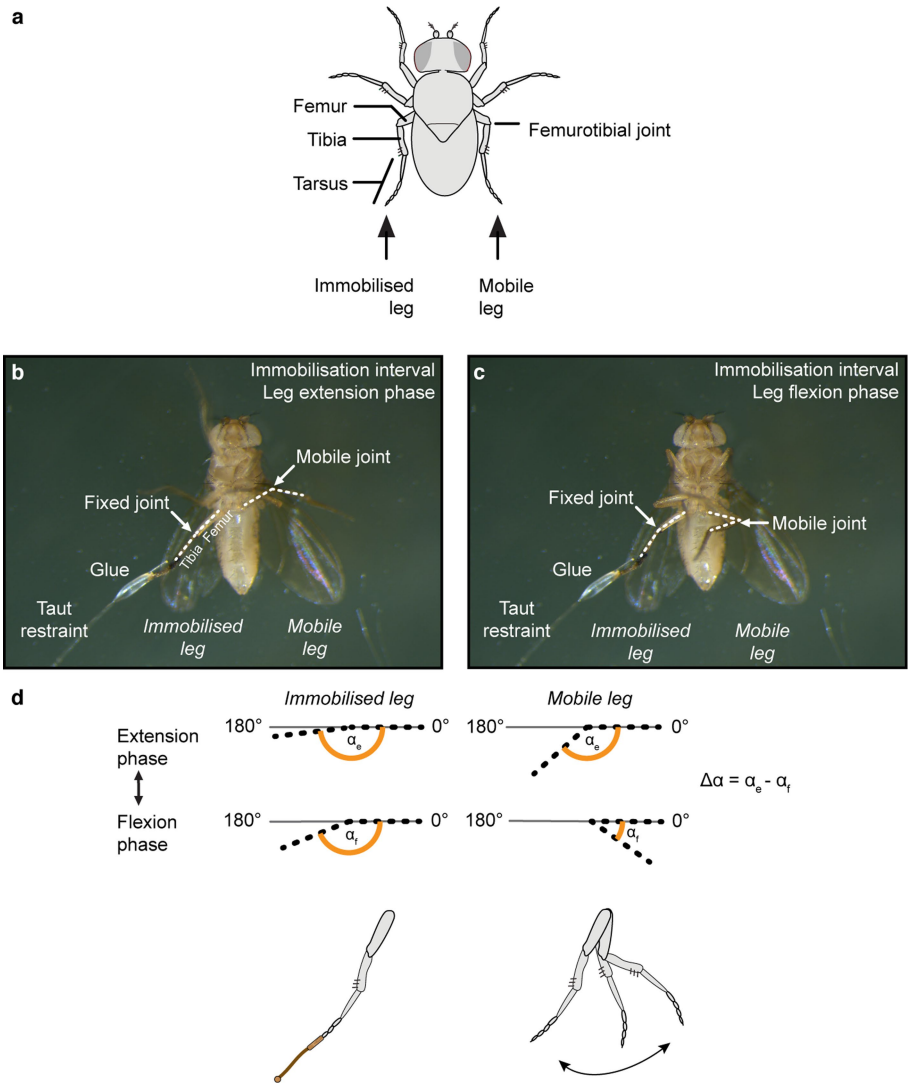

Extended Data Fig. 6 | Manipulation of leg-joint movement. a, Position of femorotibial joint in adult metathoracic leg. Adapted from ref. [67]. **b**,**c**, Adult flies were glued to a support and videotaped before, during and after the leg immobilization procedure. In the photographs the fly is displayed only during the immobilization interval, when the experimental metathoracic leg is fixed in extension with a taut restraint during the leg extension (**b**) and flexion (**c**) phases. The support plate fixation point of the restraint is not depicted in the images. The contralateral leg was allowed to move freely during all intervals of the procedure. Dashed lines indicate axes of the femur and tibia, between which the angle was determined for the immobilized and mobile leg, respectively. **d**, The motion range of the joint ($\Delta\alpha$) was determined by measuring the difference between the femoro-tibia axes angle during maximal extension (α_e) and flexion (α_f). For clarity axes of mobile leg as shown in **b**,**c** were mirrored in the illustration.

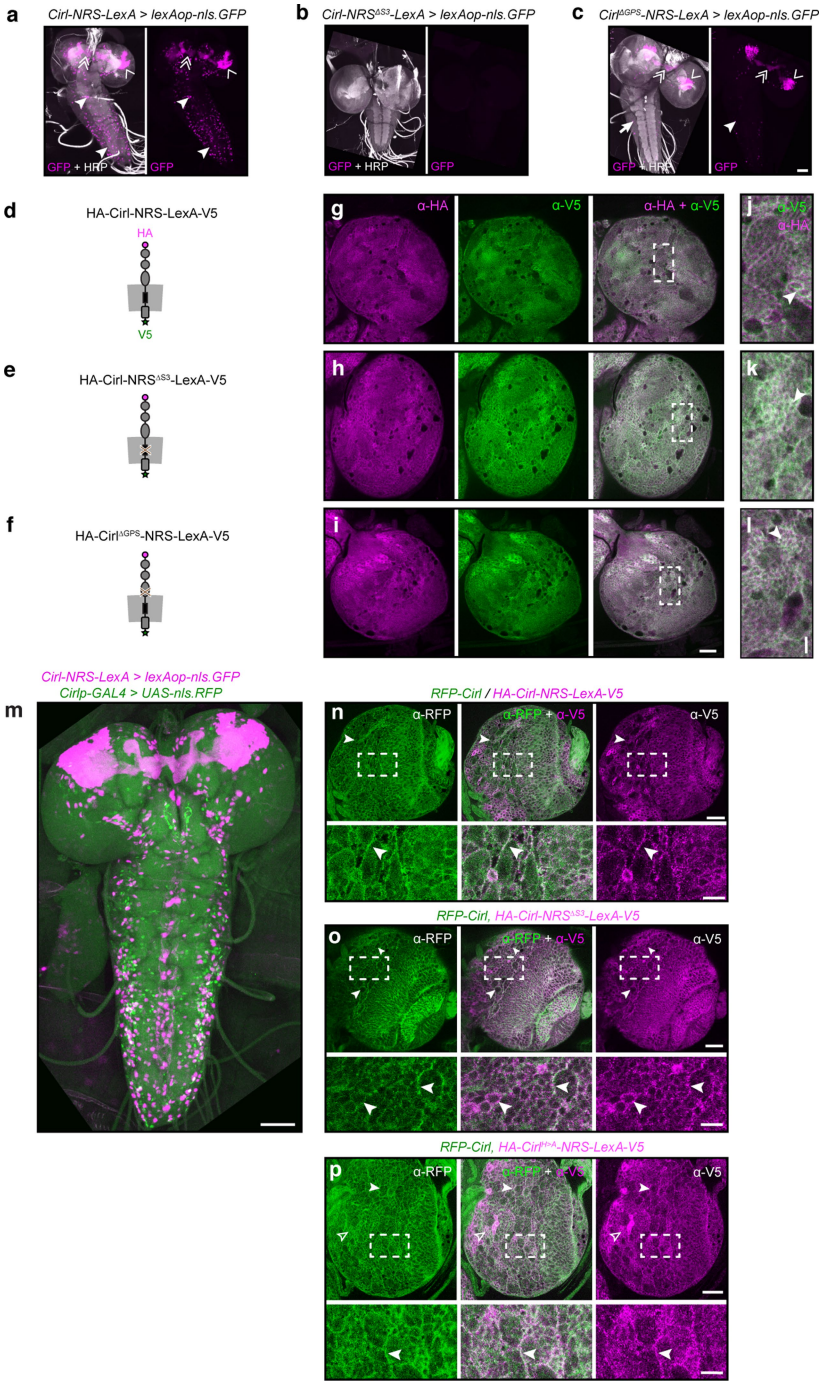

Extended Data Fig. 7 | Colocalization of Cirl-NRS-LexA and Cirl proteins. **a**–**c**, Comparisons of L3 larvae carrying wild-type (**a**), γ-secretase-resistant (**b**) or GAIN-domain cleavage-incompetent (**c**) Cirl-NRS-LexA variants showed that Cirl dissociation is receptor autoproteolysis-dependent in all neurons except in Kenyon cells (chevron) and a few individual neurons throughout the CNS (arrowheads). nls = nuclear localization sequence; Scale bars, 50 µm. **d**–**f**, Schematic illustrations of tagged NRS sensor variants. **g**–**i**, Single planes of central brain hemispheres from different NRS sensor variants immunostained using anti-HA (in magenta) and anti-V5 (in green) antibodies to visualize the ECR and C termini of NRS sensor variants (right panel). Scale bar = 30 µm. **j**–**l**, Insets of merged hemisphere images shown in **g**–**i** (dashed rectangles). N- and C-terminal NRS termini colocalize in the membrane in central brain hemisphere cells of third instar larvae (arrowheads). Scale bar = 10 µm. **m**, L3 larval brain expressing the transcriptional reporter *Cirlp-GAL4* (green) and the release sensor *Cirl-NRS-LexA* (magenta). Scale bar = 50 µm. **n**–**p**, Immunohistochemical co-staining of RFP-Cirl (green) and different Cirl-NRS variants (magenta) show colocalization of both proteins in the membrane in central brain hemisphere cells of L3 larvae (arrowheads). Dashed rectangles indicate position of areas magnified in the insets below. Scale bar = 30 µm, inset = 10 µm. All experiments independently repeated 3x with similar results.

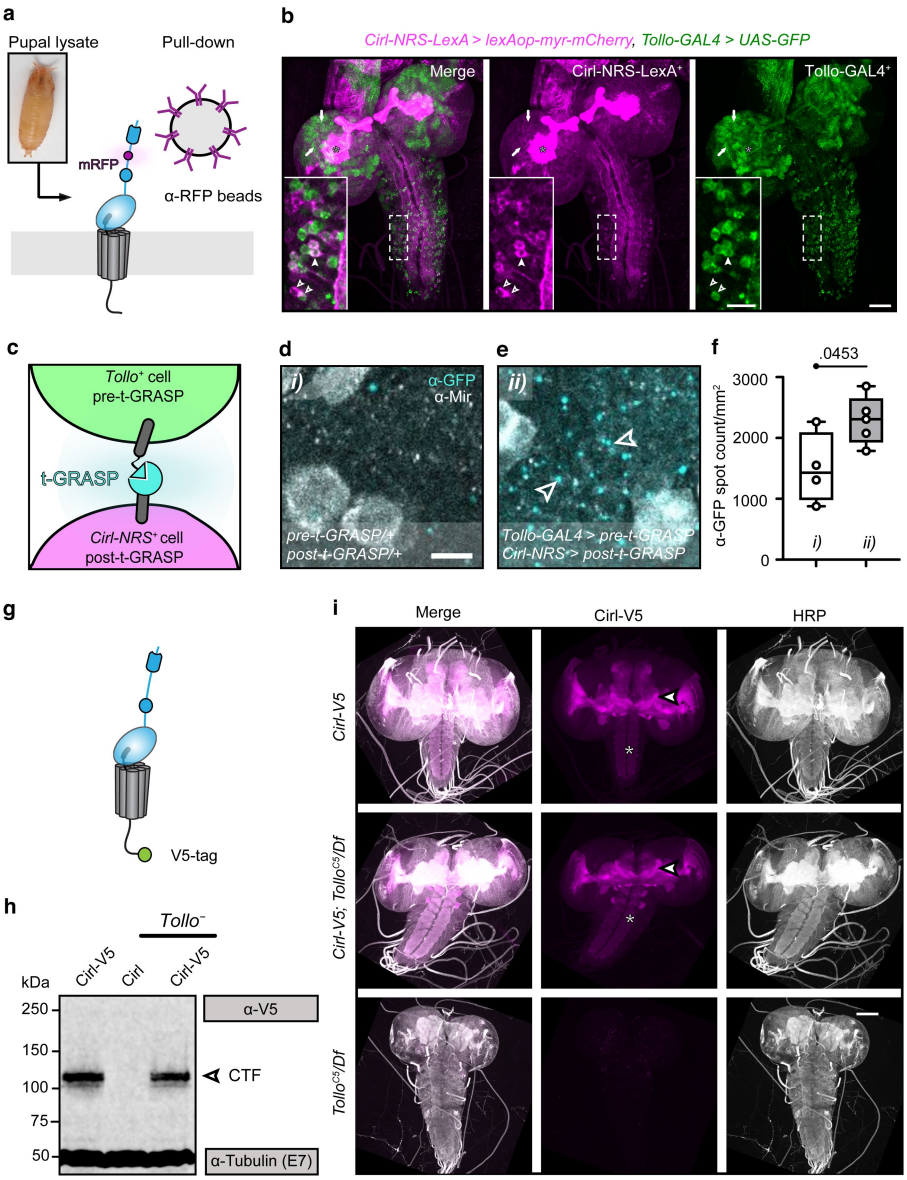

Extended Data Fig. 8 | Loss of *Tollo* does not affect Cirl expression levels or localization. a, Schematic illustration of the experimental set-up for affinity-immunoprecipitation of Cirl ligands. **b**, *Tollo-GAL4* and *Cirl-NRS-LexA* co-labelling shows co-expression of Cirl-NRS-LexA$^+$ (magenta) and Tollo-GAL4$^+$ (green) in specific areas of the brain hemispheres and VNC (inset). Strong *Cirl-NRS-LexA>lexAop-myr-mCherry* activity in the central brain is found in the mushroom body (asterisk) and in a reticular pattern in the cortex (arrows). Scale bar, 25 µm. Inset: some cells in the VNC display Tollo-GAL4$^+$/Cirl-NRS-LexA$^+$ co-labelling (closed arrowheads) while others are either Tollo-GAL4$^+$ or Cirl-NRS-LexA$^+$ (open arrowheads). Scale bar, 10 µm. Experiment independently repeated 6x with similar results. **c**, Principle of synaptic interaction screen between Tollo-GAL4$^+$ and Cirl-NRS-LexA$^+$ cells through t-GRASP. **d**,**e**, t-GRASP signals in L3 brain hemispheres enhanced by an anti-GFP immunostaining; neuroblasts visualized using anti-Mir antibody. Scale bar = 50 µm. Representative t-GRASP signals upon co-expression by *Tollo-GAL4* and *Cirl-NRS-LexA* are abundant (**e**), but hardly detectable in control flies lacking the drivers (**d**). t-GRASP signals appear to line cell boundaries (arrowheads). Scale bar, 10 µm. **f**, Quantification of t-GRASP signals in the brain indicates that Tollo-GAL4$^+$ and Cirl-NRS-LexA$^+$ cells are contacting each other. (i) and (ii) relate to images in **d** and **e**, respectively. *pre-t-GRASP/+; post-t-GRASP/+* ($n = 4$ independent flies), *Tollo-GAL4>pre-t-GRASP; Cirl-NRS-LexA>post-t-GRASP* ($n = 5$ independent flies). Data are presented in a box-whisker plot (all data points plotted; horizontal line represents median, boxes the 25th and 75th percentiles, whiskers minimum and maximum values). Data were compared with a two-tailed unpaired *t*-test (confidence interval = 95%). See also Source Data. **g**, Illustration of C-terminally V5-tagged Cirl. **h**, Western blot analysis showing similar Cirl expression levels in the presence and absence of *Tollo*. α-tubulin served as loading control. Experiment independently repeated 2x with similar results. For gel source data, see Supplementary Fig. 1h. **i**, Confocal images of Cirl expression in larval brains appears unaltered in *Tollo^{KO}*. Scale bar 100 µm. Experiment independently repeated 3x with similar results.

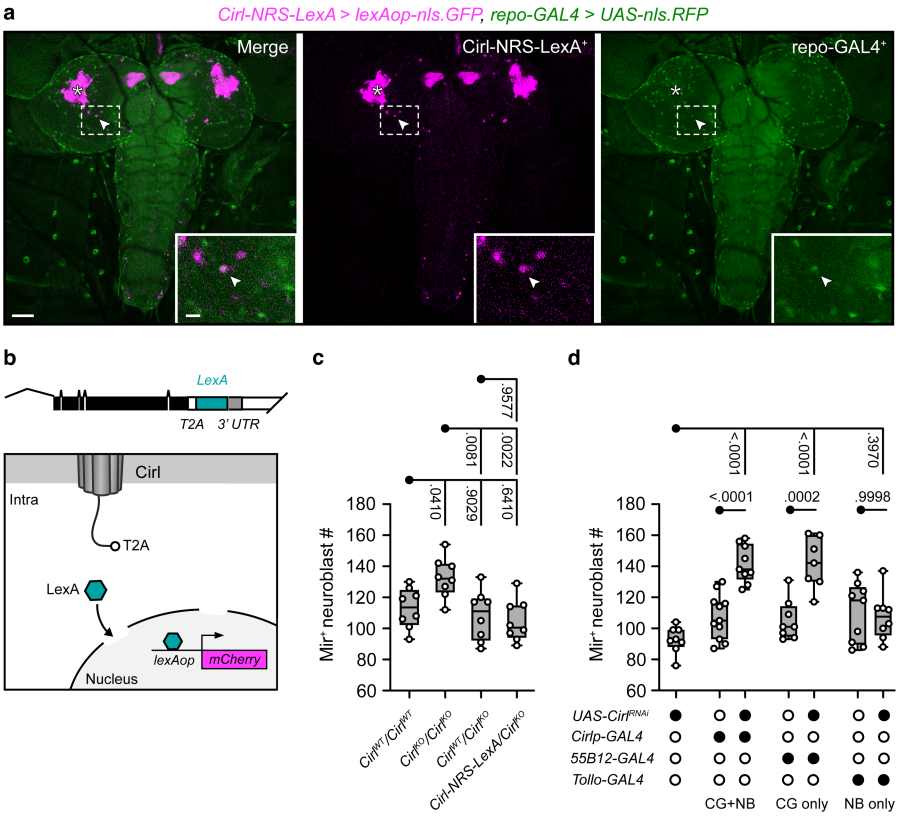

Extended Data Fig. 9 | Cirl-NTF release occurs in glial cells and is sufficient for maintaining the pool of neuroblasts. a, Single confocal plane showing sparse co-labelling of *Cirl-NRS-LexA* and pan-glial *repo-GAL4* marker in the L3 CNS (arrowhead). Boxed region magnified in inset. Asterisk indicates mushroom body. Scale bar, 50 µm; scale bar inset, 10 µm. **b**, Schematic of *Cirl-T2A-LexA* reporter allele. **c**, Cirl-NRS-LexA is sufficient for neuroblast pool size maintenance. Quantification of Mir$^+$ neuroblasts in L3 central brain ($n = 8$ independent flies per genotype). Data are presented in a box-whisker plot (all data points plotted; horizontal line represents median, boxes the 25th and 75th percentiles, whiskers minimum and maximum values). Following Shapiro–Wilk normality testing data were analysed with ordinary one-way ANOVA with Tukey's test (confidence interval = 95%). *P* values are displayed above data. See also Source Data. **d**, Cirl is only required in CG cells but not neuroblasts or GMCs to maintain a normal neuroblast pool size. Filled circle indicates presence of transgene. Quantification of Mir$^+$ neuroblasts in L3 central brain of independent flies with the genotype *UAS-Cirl^{RNAi}* ($n = 8$ independent flies), *Cirlp-GAL4* ($n = 11$ independent flies), *Cirlp-GAL4>UAS-Cirl^{RNAi}* ($n = 9$ independent flies), *55B12-GAL4* ($n = 8$ independent flies), *55B12-GAL4* ($n = 7$ independent flies), *Tollo-GAL4* ($n = 9$ independent flies) and *Tollo-GAL4>UAS-Cirl^{RNAi}* ($n = 8$ independent flies). Data are presented in a box-whisker plot (all data points plotted; horizontal line represents median, boxes the 25th and 75th percentiles, whiskers minimum and maximum values). Data were analysed with ordinary one-way ANOVA with Tukey's test (confidence interval = 95%). *P* values are displayed above data. See also Source Data.

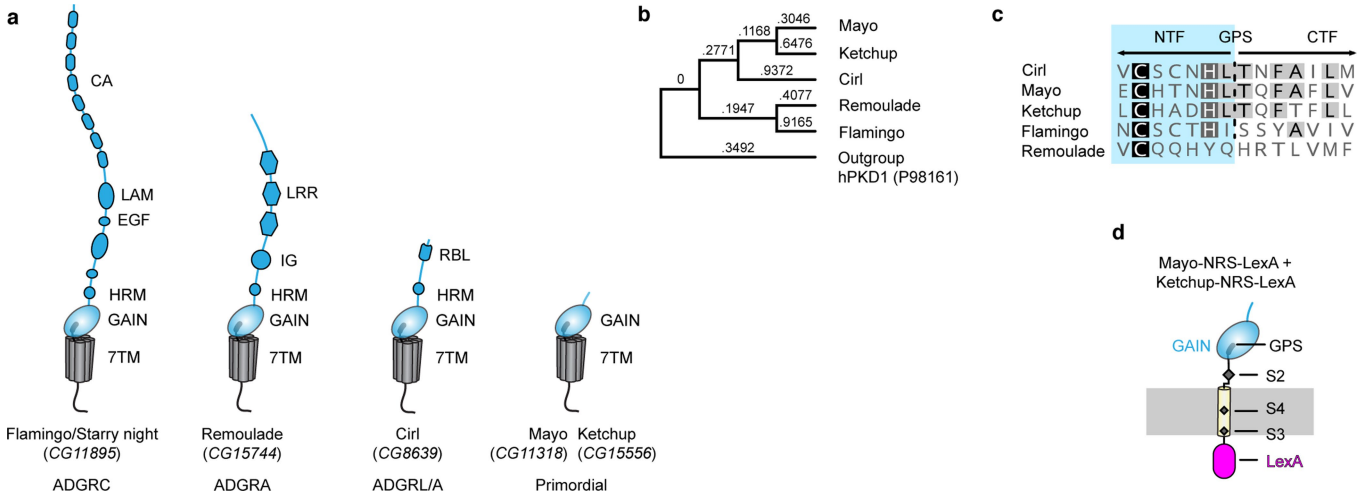

Extended Data Fig. 10 | The aGPCR family in *Drosophila melanogaster*. **a**, Structural layout of all known aGPCRs of *Drosophila melanogaster*. Domain abbreviations: 7TM, heptahelical transmembrane; CA, cadherin; GAIN, GPCR autoproteolysis-inducing; HRM, hormone-receptor motif; IG, immunoglobulin; LAM, laminin; EGF, epidermal growth factor; LRR, leucine rich repeat. **b**, Phylogenetic comparison of GAIN domain amino acid sequences using the Jukes-Cantor algorithm. Human PKD1 GAIN domain was used as an outgroup. **c**, Amino acid sequence alignment of the GPS of all fly aGPCRs shows conservation of the GPS site in four of the five receptors. Dashed vertical line indicates the site of GAIN-domain-mediated self-cleavage. NTF side boxed in blue. **d**, Structure of Mayo-NRS and Ketchup-NRS.

nature portfolio

Corresponding author(s): Tobias Langenhan, Nicole Scholz

Last updated by author(s): Jan 16, 2023

Reporting Summary

Nature Portfolio wishes to improve the reproducibility of the work that we publish. This form provides structure for consistency and transparency in reporting. For further information on Nature Portfolio policies, see our Editorial Policies and the Editorial Policy Checklist.

Statistics

For all statistical analyses, confirm that the following items are present in the figure legend, table legend, main text, or Methods section.

n/a	Confirmed	
☐	☒	The exact sample size (*n*) for each experimental group/condition, given as a discrete number and unit of measurement
☐	☒	A statement on whether measurements were taken from distinct samples or whether the same sample was measured repeatedly
☐	☒	The statistical test(s) used AND whether they are one- or two-sided *Only common tests should be described solely by name; describe more complex techniques in the Methods section.*
☒	☐	A description of all covariates tested
☐	☒	A description of any assumptions or corrections, such as tests of normality and adjustment for multiple comparisons
☐	☒	A full description of the statistical parameters including central tendency (e.g. means) or other basic estimates (e.g. regression coefficient) AND variation (e.g. standard deviation) or associated estimates of uncertainty (e.g. confidence intervals)
☐	☒	For null hypothesis testing, the test statistic (e.g. *F*, *t*, *r*) with confidence intervals, effect sizes, degrees of freedom and *P* value noted *Give P values as exact values whenever suitable.*
☒	☐	For Bayesian analysis, information on the choice of priors and Markov chain Monte Carlo settings
☒	☐	For hierarchical and complex designs, identification of the appropriate level for tests and full reporting of outcomes
☒	☐	Estimates of effect sizes (e.g. Cohen's *d*, Pearson's *r*), indicating how they were calculated

Our web collection on statistics for biologists contains articles on many of the points above.

Software and code

Policy information about availability of computer code

Data collection	N/A
Data analysis	The following software packages were used in this study: ImageJ2/Fiji v2-3-0/1.53q; Zeiss ZEN; Leica LAS X suite; Prism 9.3.1

For manuscripts utilizing custom algorithms or software that are central to the research but not yet described in published literature, software must be made available to editors and reviewers. We strongly encourage code deposition in a community repository (e.g. GitHub). See the Nature Portfolio guidelines for submitting code & software for further information.

Data

Policy information about availability of data

All manuscripts must include a data availability statement. This statement should provide the following information, where applicable:

- Accession codes, unique identifiers, or web links for publicly available datasets
- A description of any restrictions on data availability
- For clinical datasets or third party data, please ensure that the statement adheres to our policy

All datasets plotted in diagrams are available in Supplementary Table 1, interactome datasets on Cirl ligands are available via ProteomeXchange (http://proteomecentral.proteomexchange.org/) with the unique identifier PXD033873. All other data are available upon request to the corresponding authors.

Human research participants

Policy information about studies involving human research participants and Sex and Gender in Research.

Reporting on sex and gender	N/A
Population characteristics	N/A
Recruitment	N/A
Ethics oversight	N/A

Note that full information on the approval of the study protocol must also be provided in the manuscript.

Field-specific reporting

Please select the one below that is the best fit for your research. If you are not sure, read the appropriate sections before making your selection.

☒ Life sciences ☐ Behavioural & social sciences ☐ Ecological, evolutionary & environmental sciences

For a reference copy of the document with all sections, see nature.com/documents/nr-reporting-summary-flat.pdf

Life sciences study design

All studies must disclose on these points even when the disclosure is negative.

Sample size	Sample sizes were not predetermined by statistical methods. To enable statistical analyses of the in vitro datasets sample sizes of n=3 or more were used. For all assay replicates were performed as indicated in the related figure captions. For imaging data, sample sizes were limited by availability of animals of the respective genotype.
Data exclusions	No data were systematically excluded.
Replication	Number of replicates and sample sizes of displayed results are indicated in the figure legends.
Randomization	Allocation of samples (cells, animals) for data collection and analyses was random. Covariates were not relevant in this study as experimental and control experiments were performed in parallel, and flies/cells were maintained under identical rearing/culture conditions.
Blinding	Fly genotypes for neuroblast counts were blinded during data analyses, fly genotypes for expession studies could not be blinded due to regognisable specific expression patterns. Blinding for ELISA and luciferase analyses was not attempted as these are not subject to the researchers' bias due to the automated quantative readout of the assays.

Reporting for specific materials, systems and methods

We require information from authors about some types of materials, experimental systems and methods used in many studies. Here, indicate whether each material, system or method listed is relevant to your study. If you are not sure if a list item applies to your research, read the appropriate section before selecting a response.

Materials & experimental systems

n/a	Involved in the study
☐	☒ Antibodies
☐	☒ Eukaryotic cell lines
☒	☐ Palaeontology and archaeology
☐	☒ Animals and other organisms
☒	☐ Clinical data
☒	☐ Dual use research of concern

Methods

n/a	Involved in the study
☒	☐ ChIP-seq
☒	☐ Flow cytometry
☒	☐ MRI-based neuroimaging

Antibodies

Antibodies used	Primary antibodies rat-α-HA-Peroxidase (Roche, clone 3F10, #12013819001) rat-α-Mir (Abcam, CD#5-7E9BG5AF4, ab197788)

rabbit-α-HA (#C29F4; RRID: AB_10693385)
mouse-α-tubulinβ (DSHB e7, RRID: AB_528499)
mouse-α-Spectrinα (DSHB 3A9; RRID: AB_528473)
rabbit-α-HA (Cell Signaling Technology, #C29F4; RRID:AB_1549585)
rabbit-α-RFP (Antibodies-Online, RRID:AB_10781500)
mouse-α-V5 (Invitrogen, RRID:AB_2556564)
rabbit-α-GFP (Invitrogen #G10362, RRID:AB_2536526)
α-Horseradish Peroxidase conjugated with Alexa Fluor-488 (Jackson Immuno Research, #123-545-021, RRID: 2338965) or Cy3 (Jackson Immuno Research #123-165-021, RRID: AB_2338959)

Secondary antibodies
Cy5-conjugated goat-α-rabbit (Jackson Immuno Research, #111-175-144, RRID: AB_2338013)
Cy3-conjugated goat-α-rat (Invitrogen #A10522; RRID: AB_2534031)
Cy3-conjugated goat-α-rabbit (#111-165-003; RRID: AB_2338000, Jackson ImmunoResearch)
Cy3-conjugated goat-α-mouse (#115-165-146; RRID: AB_2338690, Jackson ImmunoResearch)
IRDye 680RD goat-α-rabbit (RRID:AB_2721181)
800CW goat-α-mouse (RRID:AB_2687825)
goat-α-mouse (RRID:AB_2651128)
goat-α-rabbit (RRID:AB_2651127)

Validation

For all immunohistochemistry experiments we included genetic controls (negative controls) lacking the respective biochemical tag or chromophore when engineered into the vectors by us.

We included „no primary antibody control“ (e.g. no primary mouse-V5 or rabbit-HA antibody added) for all immunohistochemistry experiments. These controls did not show signals above background fluorescence.

In addition, primary antisera were valdiated as follows:
rat anti-HA-Peroxidase, by the vendor (This antibody was verified by relative expression to ensure that the antibody binds to the antigen stated)
rat-α-Mir (Atwood and Prehoda, 2009; 10.1016/j.cub.2009.03.056)
mouse-α-tubulinβ (Devambez et al., 2017; 10.1038/s41598-017-16586-w)
rabbit-α-HA, by the vendor (This antibody was verified by relative expression to ensure that the antibody binds to the antigen stated)
mouse-α-Spectrinα (Dubreuil et al., 1987; 10.1083/jcb.105.5.2095)
rabbit-α-RFP, by the vendor (This antibody was verified by relative expression to ensure that the antibody binds to the antigen stated)
mouse-α-V5, by the vendor (This antibody was verified by relative expression to ensure that the antibody binds to the antigen stated)
rabbit-α-GFP, by the vendor (This antibody was verified by relative expression to ensure that the antibody binds to the antigen stated)
α-Horseradish Peroxidase conjugated with Alexa Fluor-488, by the vendor (This antibody was verified by relative expression to ensure that the antibody binds to the antigen stated)

To visualize neuronal membranes we used dye-conjugated-Horseradish Peroxidase (Jackson ImmunoReserach #123-545-021, #123-165-021; Jan, L Y, & Jan, Y N, 1982, https://doi.org/10.1073/pnas.79.8.2700). We used anti-miranda antibody to stain neuroblasts (abcam ab197788). According to validation experiments by the manufacturer and in Yang Ching-Po et al., 2017 (doi: https://doi.org/10.1242/dev.149500) this antibody specifically recognises neuroblasts. As loading controls for Westen Blot analyses we used alpha-Sepctrin-alpha (#3A9, DSHB) and alpha-tubulin-beta antibodies (#E7, DSHB), which reliably indicate overall protein quantity across lanes (specificity check not required for this purpose). Specificity of rabbit anti-HA-Peroxidase antibody used for ELISA was ensured using negative control samples lacking HA-tagged Cirl-NRS sensor.

Eukaryotic cell lines

Policy information about cell lines and Sex and Gender in Research

Cell line source(s)	Drosophila Schneider 2 (S2) cells, ThermoFisher Scientific, #R69007 HEK293T, German Collection of Microorganisms and Cell Culture (Braunschweig, Germany), #ACC635
Authentication	Cell lines were maintained and authenticated by the supplier, no additional authentication was performed by the authors of this study.
Mycoplasma contamination	Cell lines were regularly tested for mycoplasma contamination by the authors and tested negative.
Commonly misidentified lines (See ICLAC register)	No commonly misidentified cell line was used in this study.

Animals and other research organisms

Policy information about studies involving animals; ARRIVE guidelines recommended for reporting animal research, and Sex and Gender in Research

Laboratory animals	Third instar larvae (L3), 2-day old pupae and freshly hatched adults of Drosophila melanogaster (w[1118] wildtype strain background) were used for several experiments in this study. The complete annotated list of all fly strains used is provided in the Methods section. w1118; CirlKO {pTL803[HA-Cirl-NRS-LexA-3xV5-attB]}attPCirl w- loxP/CyO;; w1118; CirlKO {pTL804[HA-CirlΔGPS(H>A)-NRS-LexA-3xV5-attB]}attPCirl w- loxP/CyO;; w1118; CirlKO {pTL807[HA-Cirl-NRSΔS3-LexA-3xV5-attB]}attPCirl w- loxP/CyO;;

w1118; CirlKO {pTL803[HA-Cirl-NRS-LexA-3xV5-attB]}attPCirl w- loxP, 13xlexAop2-6xmCherry-HA w*/CyOGFPw-;;
w1118; CirlKO {pTL879[HA-Cirl-NRS-GAL4-3xV5-attB]}attPCirl w- loxP/CyO;;
w1118; CirlKO {pTL879[HA-Cirl-NRS-QF2-3xV5-attB]}attPCirl w- loxP/CyO;;
w1118;; MayoKO {pTL914[HA-Mayo-NRS-LexA-3xV5-attB]}attPMayo DsRed- loxP/TM3,Sb;;
w1118;; MayoKO {pTL915[HA-MayoΔGPS(H>A)-NRS-LexA-3xV5-attB]}attPMayo DsRed- loxP/TM3,Sb;;
w1118;; MayoKO {pTL917[HA-Mayo-NRSΔS3-LexA-3xV5-attB]}attPMayo DsRed- loxP/TM3,Sb;;
w1118;; KetchupKO {pTL918[HA-Ketchup-NRS-LexA-3xV5-attB]}attPKetchup DsRed- loxP/TM3,Sb;;
w1118;; KetchupKO {pTL920[HA-KetchupΔGPS(T>A)-NRS-LexA-3xV5-attB]}attPKetchup DsRed- loxP/TM3,Sb;;
w1118;; KetchupKO {pTL921[HA-Kecthup-NRSΔS3-LexA-3xV5-attB]}attPKetchup DsRed- loxP/TM3,Sb;;
w1118; CirlKO {pTL803[HA-Cirl-NRS-LexA-3xV5-attB]}attPCirl w- loxP/CyoGFPw-;;
w1118;:Cirl[108/3A.2]{attP+ loxP+}[w-] att{dCirl-NRS-lexA [w-]/CyoGFPw-;w[*]; P{w+mW.hs=GawB}MD806/TM6B,Tb
w1118; CirlKO {w+mC=pNH191[Cirl7TM-2xV5 w-]}attPCirl/CyoGFPw-;;
w1118; CirlKO {w+mC=pNH189[RFP-Cirl7TM-2xV5 w-]}attPCirl;;
w1118; CirlKO {w+mC=pNH306[Cirl1TM-V5-T2A-Gal4, Cirl7TM-V5-T2A-LexA w-]}attPCirl; Kr-Gal4
w1118; Syb::RFP w+ attP40/CyO;
w1118; CirlKO {pTL804[HA-CirlΔGPS(H>A)-NRS-LexA-3xV5-attB]}attPCirl w- loxP/CyoGFP w-;;
w1118; CirlKO {pTL807[HA-Cirl-NRSΔS3-LexA-3xV5-attB]}attPCirl w- loxP/CyoGFP w-;;
13xLexAop2-6xmCherry::HA w+ [BDSC#52272]/CyoGFPw-; 20xUAS-6xGFP w+ [attP2][BDSC#52262]
w1118; dCirl-GAL4/CyoGFPw-; P{w+mC=UAS-RFP.W}3, P{w+m*=lexAop-2xhrGFP.nls}3a /TM6B, Tb
w1118;; Df(3L)BSC578/TM6C, cu1 Sb1
w*;; tolloC5/TM6C, Tb, Sb
y1 w*; wgSp-1/CyO, P{w+mC=Dfd-EYFP}2; P{y+t7.7 w+mC=13XLexAop2-post-t-GRASP}attP2 PBac{y+mDint2 w+mC=20XUAS-pre-t-GRASP}VK00027
w*; P{w+mW.hs=GawB}MD806/TM6B, Tb1
w1118; CirlKO attPCirl w- loxP/CyoGFP w-;;
w1118; CirlKO {pTL370[CirlRescue]}attPCirl w- loxP/CyoGFP w-;;
w1118; CirlKO {pMN44[CirlH>A]}attPCirl w- loxP/CyOGFP w-;;
w1118; CirlKO {pMN4[CirlN-RFP]}attPCirl w- loxP/CyOGFP w-;;
w1118;; {w+m=pTL471[20xUAS-IVS-Cirl::3xflag]}attP2/TM3, Sb, Kr-GAL4
w1118; dCirlKO {w+mC=pTL464[Cirl-p-Gal4]}attPdCirl loxP/CyOGFPw-;;
y1 w*; wgSp-1/CyO, P{Wee-P.ph0}BaccWee-P20; P{y+t7.7 w+mC=20xUAS-6xmCherry-HA}attP2
y1w1118;;P{w+mC QUAS-mtdTomato::3xHA}26
w*;; UASt-Lifeact::GFP/TM6B, Tb
w1118; P{GMR55B12-GAL4}attP2
w*;; P{ w+mW.hs GawB}MD806/TM6B, Tb1
w*;; P{w+m*=GAL4}repo/TM3, Sb1
yw; PBac{y+mDint2w+mC 13xlexAop2-6xmCherry::HA}VK00018/CyO;
yw;; P{y+t7.72w+mC 20xUAS-6xGFP }attP2
yw;20xUAS-6xGFP; lexAop-myr::mCherry
w1118;;UAS-RFPnls/TM3, Sb1
w1118;; P{w+mC lexAop-2xhrGFP.nls}3a
; ok6-Gal4 w+;
w1118; P{w+m*=lexAop-2xhrGFP.nls}2a;;
w1118; +; MayoKO {pTL789 [Mayo-p-GAL4-attB]}attPMayo DsRed- loxP /TM3, Sb;;
v1; Krlf-1/CyO; P{y+t7.7 v+t1.8=UAS-TransTimer.v+}attP2
w1118; phiC31{KK108383}v100749

Wild animals	No wild animals were used in this study.
Reporting on sex	Sex of animals was not considered in this study.
Field-collected samples	No field-collected samples were used in this study.
Ethics oversight	No ethical approval or guidance was required for this study.

Note that full information on the approval of the study protocol must also be provided in the manuscript.